

# MULTIPLE AMORPHOUS–AMORPHOUS TRANSITIONS

THOMAS LOERTING

*Institute of Physical Chemistry, University of Innsbruck, Innrain 52a, A-6020  
Innsbruck, Austria*

VADIM V. BRAZHKIN

*Institute for High Pressure Physics, Troitsk, Moscow Region, 142190 Russia*

TETSUYA MORISHITA

*Research Institute for Computational Sciences (RICS), National Institute of  
Advanced Industrial Science and Technology (AIST), Central 2, 1-1-1 Umezono,  
Tsukuba, Ibaraki, 305-8568 Japan*

## CONTENTS

- I. Introduction
- II. Covalent Oxide Glasses
  - A. Silica
  - B. Other Oxide Glasses
- III. Water
  - A. Preparation of Amorphous Ices
  - B. Structural Information
  - C. Irreversible Structural Transitions by Heating at 1 Bar
  - D. Reversible in situ Structural Transitions
  - E. Are the Amorphous Solids Glasses or Nanocrystallites?
- IV. Semiconductors
  - A. General Comments
  - B. Amorphous Si

C. Amorphous Ge

D. Liquid Si and Ge (l-Si and l-Ge)

V. Discussion and Conclusions

Acknowledgments

References

## I. INTRODUCTION

The amorphous solid state of matter has traditionally received much less attention than the crystalline solid state [1–4]. By contrast to crystalline solids, which are ordered and can be defined using a periodically repeated unit cell, amorphous solids are disordered on long-range scales. Amorphous solids show a short-range order, e.g., tetrahedrality, which is similar to the short-range order found in crystalline solids. However, long-range order in amorphous solids does not exist because order typically disappears at distances of 20–50 Å. Because of their inherent disorder, amorphous solids are metastable with respect to the well-ordered crystals. The difference in Gibbs free energies is often called “excess free energy.” Many methods of producing amorphous solids are available using the gas, the liquid, and the solid as starting materials. All of them share the principle that excess free energy has to be provided, e.g., by mechanical, thermal, or chemical treatment, which is taken up by the material [5]. Amorphous solids are often divided in two subgroups—glasses and nonglassy amorphous solids. One of the most traditional routes of producing glasses is by cooling the liquid below the melting temperature without crystallizing it [6, 7]. Thus, glasses are synonymously also called vitrified liquids. After reheating a glassy solid, it turns into a supercooled liquid above the glass→liquid transition temperature  $T_g$ . In the transition region from the glassy solid to the supercooled liquid near  $T_g$  the microscopic structure does not change—rather the relaxation dynamics change [8]. Whereas glasses are nonequilibrium states, which slowly relax toward the metastable equilibrium on the experimental time scale, the metastable equilibrium is reached within the experimental time scale in case of supercooled liquids. By contrast, a nonglassy amorphous solid does not turn into a supercooled liquid during heating. Instead, either it remains in the amorphous solid state or it crystallizes. As an explanation why these amorphous solids behave unlike glasses, often the concept of “nanocrystalline” material is invoked [9–11], which basically implies that the material is made of a huge number of very small crystal grains, each of which contains on the order of a few hundred molecules. In this view, the sharp Bragg peaks in scattering experiments characteristic of crystalline material are not observed because they are massively broadened because of the small crystal sizes. For example, the X-ray pattern cannot be distinguished then from true glassy material, and thus, the “nanocrystalline” material looks “X-ray amorphous.” Although both “nano-

crystalline” and “glassy” solids do not show long-range order, they can be distinguished in terms of how the short-range order disappears at intermediate ranges [12]. In the glassy state, the order disappears more or less continuously by variation of interbond angles and (to a lesser extent) interatomic distances. In the “nanocrystalline” state, the order is lost more or less discontinuously at the grain boundaries—almost no variation of interbond angles and interatomic distances is observed inside the nanocrystals, but strong variation exists at the intergrain boundaries (although the size of the nanograin and the intergrain boundary may be compatible to each other). Instead of grain boundaries, defective crystals distorted by linear defects (disclinations, dispirations, and displanations) have been considered [13]. So, in amorphs one speaks about three distance ranges as follows: (1) the short-range order, which typically reaches the direct neighbors of a central atom or molecule, i.e., the first coordination sphere (sometimes the second coordination sphere); (2) the intermediate range order, which typically encompasses the second to the fifth through seventh coordination spheres, where the loss of order occurs [14–20]; and (3) the long range beyond the fifth through seventh coordination spheres, where there is no order.

During variation of pressure and/or temperature, the amorphous solids may experience different processes, which can be superimposed as follows: (1) elastic reversible behavior, that is, the connectivity in the network remains the same—just isothermal compression and/or thermal expansion take place; (2) inelastic behavior associated with the change of intermediate-range order; (3) inelastic behavior associated with a change of short-range order including coordination changes in the first through second spheres; and (4) irreversible structural relaxation associated with the equilibration process toward the metastable equilibrium. Whereas (1) is found for any material and (4) is related to the kinetics of relaxation, (2) and especially (3) represent structural transitions governed by the laws of thermodynamics analogous to phase transitions for crystals. In this sense, structural transitions in amorphs have been called “phase” transitions, even though amorph (nonequilibrium nature) and phase (equilibrium nature) are in direct contradiction. Glasses and amorphous solids are nonergodic, non-equilibrium states, and a strict physical meaning of the “phase” can be applied to them only conditionally (“metastable phase”) [21]. The use of terminology reserved for true equilibrium transitions (phase, latent heat, first-order nature, nucleation, etc.) seems to be justified in view of the experimental finding that the metastable amorphous states can be stabilized for very long times, if not infinitely, under suitable conditions [i.e., process (4) can be suppressed effectively]. That is, the term “phase” can be applied conditionally for “metastable phase.” In this sense, the amorphs can be viewed to be in a metastable quasiequilibrium rather than in nonequilibrium. Such a metastable quasiequilibrium allows for the definition of a coexistence line, where Gibbs free energies of two amorphous states are identical, and the possibility of “first-order” transitions that involve

jump-like changes in entropy, volume, and enthalpy arises. Also the possibility of a critical point located at the end of the coexistence line arises. Another complicating circumstance with respect to amorphous solids and glasses is that the transformations between different “phases” during the experimental times occur, as a rule, under conditions that are far from equilibrium; these transformations are determined by kinetic parameters, much like low-temperature phase transitions with a large hysteresis found in crystals [22].

Structural phase transitions in crystals under changes of the P,T-parameters are a well-studied phenomenon from both the experimental and theoretical viewpoints. The concept of “polymorphism,” i.e., the occurrence of more than one crystal structure for a single component, is a well-known and traditional concept. For many components, the phase diagram of stable polymorphs has been constructed and shows lines in the P,T diagram, where two polymorphs can coexist in thermodynamic equilibrium. Crossing these lines then causes a sharp structural transition, i.e., a change of short-range order in the unit cell [very much like mechanism (3)] [23]. However, the concept of “poly-amorphism,” i.e., the occurrence of more than one amorph, and structural transitions between these amorphs is relatively new and not well understood. Disordered systems possess additional, more essential characteristics that differentiate them from crystals, namely, the inhomogeneity of their structure and the dispersion of their properties on the scales smaller than the correlation length of a medium order in disordered systems. For this reason, the disordered systems follow two scenarios of phase transformations: Either they can experience a first-order phase transition, provided the minimum size of a nucleus of an emerging phase is larger than the correlation length of a disordered state, or, by contrast, they undergo smeared changes (at all temperatures) [24]. For the smooth transitions, there is a series of intermediate states, each being in compliance with the condition of minimum of the Gibbs free energy. This particular scenario cannot be realized in crystals, where just two definite phases exist whose macroscopic mixture may be thermodynamically equilibrated in the transition point only. Thus, the experimental observation of sharp changes of the structure and properties in the disordered systems, as opposed to crystals, is a necessary but insufficient evidence for a first-order transition, for there always remains the possibility of this transition occurring in a fairly narrow but finite P,T-interval. As a result, the principal evidence for the first-order transition in the disordered media is the observation of a macroscopic mixture of phases during transition [22].

The concept of a *single* structural transition in amorphous material, i.e., an amorphous–amorphous transition, was coined in 1985 by Mishima et al. [25] on the example of water. Today, in many respects the nature of pressure- and/or temperature-induced transformations in glasses and amorphous solids remains unclear. In most cases, the pressure treatment of glasses and amorphous solids results in residual densification. In the process, the densified glasses and

amorphous solids do not undergo any significant change in a short-range order (coordination number  $Z$ ) as a rule; it is only amorphous network topology (ring statistics, etc.) that varies. Nevertheless, there are some examples of coordination transformations in amorphous solids, glasses, and liquids, which can take place in a sharp manner or smeared over a wide pressure and temperature range, e.g., amorphous  $\text{H}_2\text{O}$ ,  $\text{SiO}_2$ ,  $\text{GeO}_2$ ,  $\text{B}_2\text{O}_3$ , Si, Ge (for references, see Sections II through IV),  $\text{A}_3\text{B}_5$ -compounds, Se, S, P,  $\text{AlCl}_3$ ,  $\text{ZnCl}_2$ ,  $\text{ZnSe}$ , amorphous irradiated zircon [26], some metallic glasses (e.g.,  $\text{Ce}_{45}\text{Al}_{55}$ ) [27], and in aluminates [28]. These examples, where a coordination transformation in the amorphous solid can be observed, are the candidates for possible *multiple* amorphous–amorphous transitions, which are the focus of the current review. Among these candidates, some evidence has been accreted for a possible multiple nature of amorphous–amorphous transitions. Therefore, we discuss covalent oxide glasses such as  $\text{SiO}_2$ ,  $\text{GeO}_2$ , and  $\text{B}_2\text{O}_3$  in Section II,  $\text{H}_2\text{O}$  in Section III, and the semiconductors Si and Ge in Section IV. Interestingly, a good correlation exists between the few glasses that show coordination transformations and the few liquids known to show anomalous behavior, such as an apparently diverging heat capacity and compressibility during supercooling, the negative melting slope in the P-T phase diagram, or a density maximum. Although the possibility of structural transformations under compression in some glasses is beyond doubt, the question whether the phase diagram of the glass (and melt) is a shifted reflection of the pressure–temperature phase diagram of the crystal remains to be answered. Multiple-phase transitions under pressure for one substance in the crystalline state are possible often; whether multiple structural transformations can similarly be observed in a respective glass and melt is a matter of debate. Whereas there is barely any experimental information on true multiple liquid–liquid transitions (except for the case of AsS [29]), simulations have suggested the possibility of multiple first-order liquid–liquid transitions [30–36].

Although we focus here on the *status quo* concerning the debated aspect of multiple amorphous–amorphous structural transitions, we want to emphasize that there are numerous reviews on the topic of polyamorphism and single amorphous–amorphous transitions worth reading [37–48].

## II. COVALENT OXIDE GLASSES

### A. Silica

Of greatest interest is the study of pressure-induced transformations in such an archetypical glass as a- $\text{SiO}_2$ . Besides the fundamental importance of research on transformations in disordered media, a deeper insight into the transitions that occur in a- $\text{SiO}_2$  and other amorphous and liquid silicates is of much importance for the physics of the Earth and planetary interiors. Thus, we pay the most

attention to the  $\alpha$ - $\text{SiO}_2$  study, whereas other oxide glasses such as  $\text{GeO}_2$  and  $\text{B}_2\text{O}_3$  will be considered more concisely.

Silica ( $\text{SiO}_2$ ) is the substance whose properties and phase-transition behavior are vital for understanding the puzzling processes and phenomena existing in the Earth's upper mantle and in Earth-like planets [49, 50]. Silica, being one of the most abundant components of the Earth, "plays a major role in the deep interior, both as a product of chemical reactions and as an important secondary phase" [51]. The equilibrium pressure-temperature (P-T) phase diagram of silica is relatively well understood, and it has been extensively reviewed elsewhere [51] (Fig. 1). Under compression, the  $\text{SiO}_2$  crystal undergoes a set of transitions from  $\alpha$ -quartz (the silicon atom coordination number relative to oxygen atom number,  $Z = 4$ )  $\rightarrow$  coesite ( $Z = 4$ ) ( $P \sim 3$  GPa)  $\rightarrow$  stishovite (rutile structure) ( $Z = 6$ ) ( $P \sim 9$  GPa)  $\rightarrow$   $\text{CaCl}_2$ -structure type ( $Z = 6$ ) ( $P \sim 70$  GPa)  $\rightarrow$   $\alpha$ - $\text{PbO}_2$ -structure type ( $Z = 6$ ) ( $P \sim 100$  GPa) – pyrite-structure type ( $Z = 8$ ) ( $P \sim 260$  GPa)[51–63].

The behavior of the  $\text{SiO}_2$  glass under pressure has been intensely studied as well [39, 53, 64–83]. It was established long ago that the high-pressure, high-temperature treatment causes a significant residual densification of silica glass

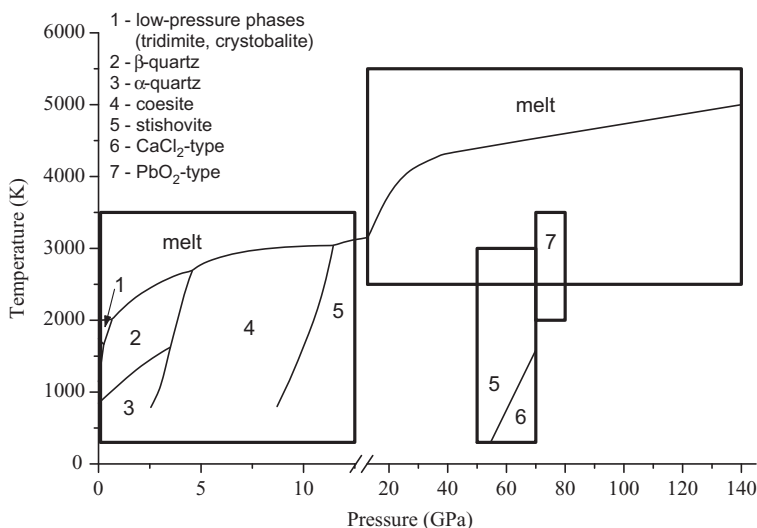


**Figure 1.** Schematic high P-T phase diagram of  $\text{SiO}_2$  determined from static compression experiments. Rectangles are areas already studied. The bottom left rectangle (with 1–5 phases) is part of a diagram by both in situ and quenching techniques in a large volume press apparatus [51–54]. The upper right rectangle was studied by shock-wave and laser heating in diamond anvil study of the melting curve [55–57]. The bottom right middle rectangle with 5/6 is the study (laser heating with diamond anvils) of stishovite to  $\text{CaCl}_2$  transition [58] with a line of 5/6 phase transition [59]. The bottom right rectangle with 7 is an area investigated by which includes Dubrovinsky et al. [60], laser heating with diamond anvils.

[14, 66–68, 70, 71, 76, 84–87]. The maximum densification of 18–20% is achieved after a pressure of 16–20 GPa—room temperature treatment or after 5–8 GPa—800–1000 K treatment. The densified glasses have predominantly tetrahedral coordination of silica atoms,  $Z \sim 4\text{--}4.5$  [14, 71, 88]. Elastic moduli and optical characteristics of densified glasses are distinctly different from those of pristine silica glasses.

The extensive studies on the structure [72, 89] and Raman and Brillouin spectra [68–70, 73], as well as computer simulation results [77–82] have revealed that in the 8–50 GPa pressure range and at room temperatures, the silica glass is subject to a broad transformation accompanied by a change in the short-range order structure and an increase in the coordination number from 4 to 6. It should be noted that during coordination transformation at intermediate pressures, many silicon atoms have a fivefold coordination. The main part of the transformation takes place in a narrower pressure range of 10–40 GPa.

The earlier data did not shed light on how closely this coordination transformation is related to residual densification of the glass. Another unanswered question was whether glass densification after 20 GPa pressure at room-temperatures treatment and the one at 5–8 GPa and high-temperatures treatment are of a similar nature.

Recent years have witnessed a significant advance in the understanding of the behavior of glassy silica under compression. By using a strain gauge technique, direct in situ measurements of the relative volume of the glass in a wide range of pressures (0–10 GPa) and temperatures (30–730 K) have been conducted (see Fig. 2) [90]. It has been found that at increased temperatures and pressures of 4–8 GPa, the  $\alpha\text{-SiO}_2$  glass undergoes a transformation accompanied by moderate volume changes of 2–7%, depending on the pressure. The computer simulation data [91, 92] perfectly fit those obtained by volumetric measurements (see Fig. 3). Here, we note that the data in Ref. [85] on the existence of a sharp volumetric anomaly ( $\sim 20\%$ ) at 3.6 GPa and 850 K are not corroborated by the results of other independent measurements. High residual densification ( $\sim 20\%$ ) in the glasses after decompression is caused by a considerably lower (by almost two times) compressibility of a densified glass [90]. Thus, the position in the  $T,P$ -plane of the zone of the transformation responsible for densification was determined (Fig. 4). A recently conducted in situ structural study on the  $\text{SiO}_2$  glass under high-pressure, high-temperature conditions [17] (see Fig. 5) as well has revealed the existence of this transformation region, which is in perfect agreement with the volumetric data (see Fig. 4). The computer simulation data [91, 92] and in situ X-diffraction study [17] have allowed us to clarify the nature of this transformation. The coordination number during this transformation changes insignificantly, whereas the topology of tetrahedron connectivity substantially changes toward more efficient packing of the tetrahedra. Thus, the changes during this transformation primarily affect the

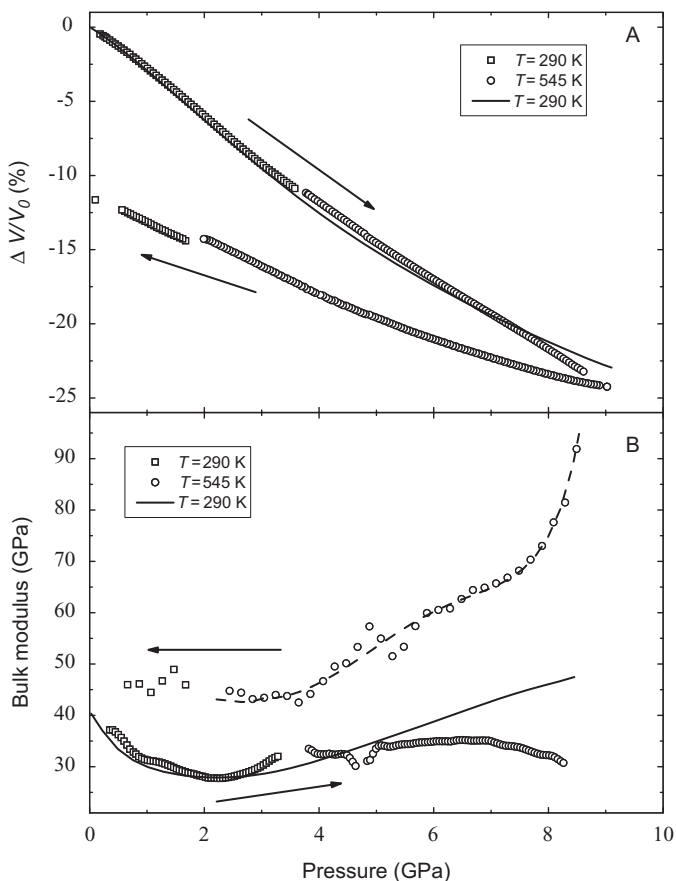


**Figure 2.** Relative change of a-SiO<sub>2</sub> volume in the compression and decompression cycles at 545 K (a) and the corresponding bulk modulus obtained by the numerical differentiation of volume curves (b). The data corresponding to the a-SiO<sub>2</sub> compression at room temperature are given for the comparison (from Ref. [90]).

intermediate-range order rather than the short-range one. In terms of the “rigidity percolation” [93], the transformation of the amorphous network with floppy modes toward the rigid network occurs [92]. The analysis of structural data has revealed that the number of small rings in the network increases during transformation; this change in the ring statistics leads to the decrease in the number and size of interstitial voids in the network. Apart from a change in the intermediate-range order, the first transformation also involves a change in the coordination of some part of silicon atoms in the fivefold and sixfold coordination states.

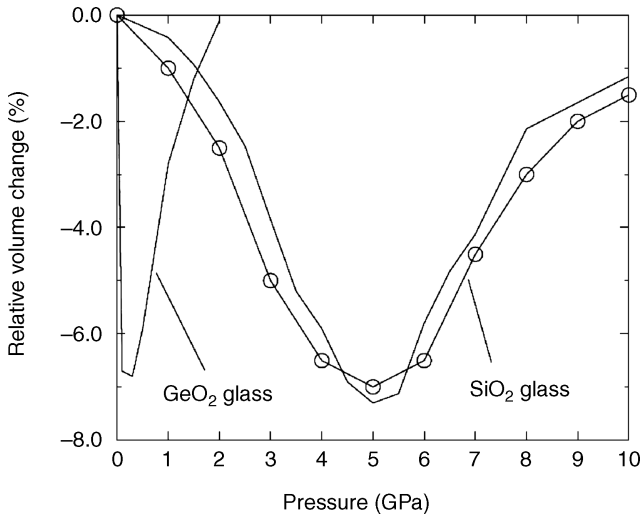


**Figure 3.** Temperature-induced densification in  $\text{SiO}_2$  and  $\text{GeO}_2$  glasses from Ref. [91]. A circled line is the experimental results; solid lines are the results from MD simulation.

Thus, the first transformation in  $\text{a-SiO}_2$  happens with a small change in the coordination number and is irreversible at room temperatures, which gives rise to residual densification (see Fig. 4). The second transformation, accompanied by the further increase of the first coordination number up to  $Z = 6$  and occurring already within the rigid network, takes place at higher pressures; it is almost independent of the temperature (see Fig. 4) and is nearly fully reversible. At room temperature, these two transformations significantly pressure overlap, whereas at higher temperatures, they can be conditionally separated.

The pressure range for the second transformation is still debatable. Note that the recent study on the bonding changes in the  $\text{SiO}_2$  glass conducted by using an inelastic X-ray scattering technique [94] gives an unreliable estimate of the degree of coordination transformation. According to Ref. [94], the transformation in the  $\text{SiO}_2$  glass to the sixfold coordination state of silicon atoms is completed at  $P \sim 20$  GPa. At the same time, the direct structural study of the  $\text{SiO}_2$  glass indicates that this coordination transformation is not completed even at  $P \sim 40$  GPa [72, 89]. At  $P \sim 18$  GPa, the coordination changes only begin [17]. A very recent inelastic X-ray Si L-edge scattering study has revealed that there is no domination of six coordinated Si atoms even at 74 GPa [95]. Fukui et al. [95] suggested that a significant fraction of five coordinated Si atoms exist up to the highest pressures. Thus, the assessments of the degree of coordination transformation in glasses made from inelastic X-ray scattering data (e.g., Refs. [94, 96, 97]) should be treated with caution.

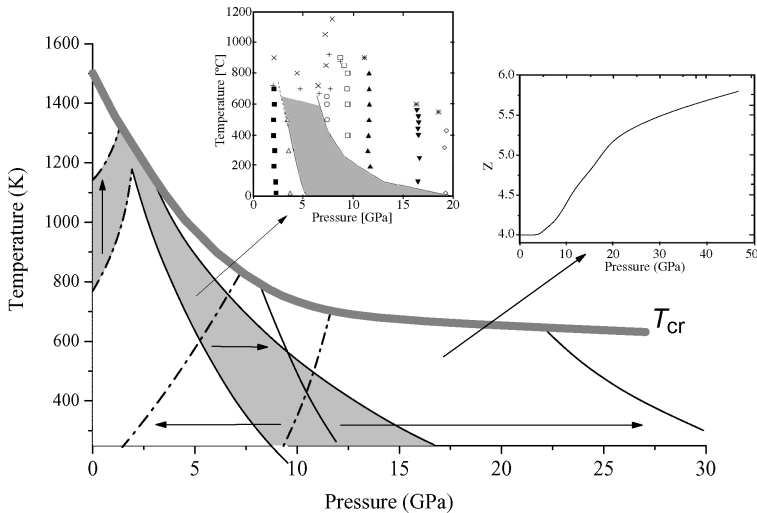


**Figure 4.** Phase diagram for the transformations of glassy SiO<sub>2</sub> according to the volumetric data from the Ref. [90]. These data are evidence for the two transitions: between the ordinary glass and densified rigid network state of glass with a small increase of coordination (the gray regions correspond to the direct and reverse transitions) and between densified state of glass and six-fold coordinated phase (nonhatched regions). The regions of direct transitions are bounded by the solid lines, and the regions of reverse transitions are bounded by dot-and-dash lines. The arrows show the directions of the corresponding transitions. The insets show the region of the first transition according to the structural study of Ref. [17] (giving with the authors' permission) and change of Si-atoms coordination during the second transition according to the computer simulation study from Ref. [80].

We note that the first transformation results in the formation of a rigid unstressed state of the amorphous network [91]. As the coordination number increases, the amorphous network becomes overstressed and overconstrained. In the case of a high atomic coordination, bond length and angle fluctuations, which are intrinsic for amorphous network, cost very high elastic energy. This leads first to higher transformation pressures as compared with crystalline prototypes and, second to the impossibility of retaining a high coordination number after decompression, which is another fact that strongly differentiates the glasses from their crystalline counterparts. Finally, these high elastic stresses in overconstrained amorphous networks cause a higher tendency to nanocrystallization of such glasses.

This is, even to a greater extent, true of oxide glasses with the coordination number  $Z > 6$ . It is obvious that with another increase in pressure to  $P \sim 1$  Mbar (the stability region of an  $\alpha$ -PbO<sub>2</sub> structure type), the coordination number in glassy silica should slightly rise [98] and approach eight at  $P \sim 2$ –3 Mbar (the stability region of a pyrite-like structure of crystalline silica). This state of the

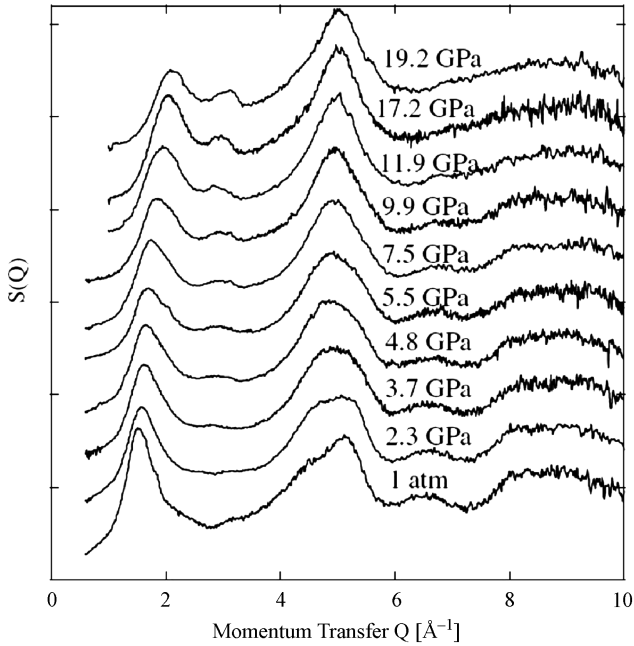


**Figure 5.** The pressure dependence of the structure factor for  $\text{SiO}_2$  glass at room temperature (from Ref. [17] with the authors' permission)

glass should be overstressed even more and should have a strong tendency to crystallization at nanoscales.

The presence of several structural phase transformations in the glassy state permits suggesting the respective structural changes in the melt. Thus, for example, in liquid  $\text{SiO}_2$ , the smooth transition with a change in the intermediate-range structure at  $P \sim 3\text{--}5$  GPa is manifested in the degree of densification of glasses obtained by quenching from melt under pressure [99], whereas the other transition is associated with a considerable rearrangement of the atomic short-range order and accounts for the anomalies of the properties of the  $\text{SiO}_2$  melt [100–105].

## B. Other Oxide Glasses

The  $\text{SiO}_2$  glass seems to be the most well-known glass but is not the only one to reveal the complicated behavior of its structural characteristics under compression. The  $\text{GeO}_2$  substance is analogous to  $\text{SiO}_2$ . The P,T diagram of  $\text{GeO}_2$  is similar to that of  $\text{SiO}_2$  (in fact, even more simple as it lacks many four coordinated phases, which includes a coesite-like one). A rutile-like phase of  $\text{GeO}_2$  ( $Z = 6$ ) transits to a  $\text{CaCl}_2$  structure type ( $Z = 6$ ) ( $P \sim 30$  GPa), then to an

$\alpha$ -PbO<sub>2</sub>-structure type ( $Z = 6$ ) ( $P \sim 50$  GPa), and finally to a pyrite-like structure ( $Z = 8$ ) ( $P \sim 85$  GPa) [63, 106, 107]. As with a-SiO<sub>2</sub>, the P,T-treatment of the GeO<sub>2</sub> glass brings about residual densification of  $\sim 14$ – $16\%$  without a significant change of short-range order coordination [16, 108].

The coordination transformation in glassy GeO<sub>2</sub> under compression with an increase in  $Z$  from 4 to 6 takes place in the 5–20-GPa pressure range, which is attested by both experimental data of the extended X-ray absorption fine structure (EXAFS) [109], volumetric [76, 110], and X-ray diffraction [111, 112] measurements, as well as computer simulation result [113, 114]. The coordination number in  $\alpha$ -GeO<sub>2</sub> rises nonmonotonically with pressure: At  $P \sim 9$ – $10$  GPa, the rate of rise of the  $Z$  value slows down [112]. According to Guthrie et al. an intermediate fivefold coordinated state of  $\alpha$ -GeO<sub>2</sub>, exists; however, it is more likely that this intermediate state includes Ge atoms of different coordinations, of 4, 5, and 6 [113, 114]. Recent structural studies on  $\alpha$ -GeO<sub>2</sub> performed simultaneously at high pressures and temperatures obtained at isobaric heating [115] and isothermal pressure runs [116] have revealed a complicated picture of structural changes. Similar to a-SiO<sub>2</sub>, the a-GeO<sub>2</sub> substance in the region of moderate pressures (1–4 GPa) and high temperatures (400–600 K) experiences the intermediate-range order changes accompanied only by an insignificant increase in the coordination number [115, 116]. The computer simulation study of the GeO<sub>2</sub> glass has also revealed a transition to the rigid network state at heating at  $P \sim 1$  GPa [91] (see Fig. 3).

Thus, for a-GeO<sub>2</sub> at high temperatures, we may conditionally consider the existence of two overlapping structural transformations under compression. It is obvious that at additional increases in pressure, a-GeO<sub>2</sub> is bound to undergo, similarly to a-SiO<sub>2</sub>, transformations accompanied by the rise in the coordination number to eight [98]. Glassy GeO<sub>2</sub> oxides with  $Z \sim 6$  and  $Z \sim 8$  are overstressed and cannot be quenched to normal pressure conditions.

The presence of several structural phase transformations in glassy GeO<sub>2</sub> suggests the respective structural changes in the melt, which is already partially confirmed by both experimental study [117] and computer simulation study [118].

B<sub>2</sub>O<sub>3</sub> represents an archetypical oxide glass alongside such glasses as SiO<sub>2</sub> and GeO<sub>2</sub> [119], with the important difference that at the ambient conditions, the structural units are planar BO<sub>3</sub> triangles as opposed to tetrahedra. As was found long ago [120, 121], pressure-treated B<sub>2</sub>O<sub>3</sub> glasses show residual densification  $\Delta\rho/\rho \sim 5$ – $10\%$ , which depend on the pressure-temperature conditions of treatment. The ex situ studies of densified glasses point to the breakup of the boroxol rings in the glass structure and to the buckling of the “ribbons” formed by the BO<sub>3</sub> triangles, without any significant coordination change of the boron and oxygen atoms [122, 123]. The in situ investigations of B<sub>2</sub>O<sub>3</sub> glass under pressure have been performed using Raman and Brillouin spectroscopies [124–126] and through inelastic X-ray scattering spectroscopy

[97]. In addition, there have been attempts to examine the  $B_2O_3$  glass under pressure by molecular dynamics computer simulation, using empirical interatomic potentials [127, 128]. According to the data of Nicholas et al. [125],  $B_2O_3$  glass under compression experiences a transformation in the pressure range  $P \sim 6\text{--}15$  GPa; according to Ref. [97]  $B_2O_3$  glass, under compression, features a considerable change in the bonding type in the  $6\text{--}20$ -GPa pressure range. These changes were attributed to the modification of the short-range order in glass, with the coordination of boron atoms increasing from 3 to 4 in a similar way to crystalline phases.

We have recently reported the results of the in situ diffraction experiments and the in situ volumetric measurements, and we have complemented them with the data from ab initio calculations [129].

The behavior of  $B_2O_3$  glass under pressure is in a certain sense similar to the behavior of other archetypical oxide glasses,  $a\text{-SiO}_2$  and  $GeO_2$ . Under pressure,  $B_2O_3$  glass equally features two overlapping diffuse transformations (see Fig. 6). The first transformation is irreversible at room temperature without the change in the first coordination number and is accompanied by the change of

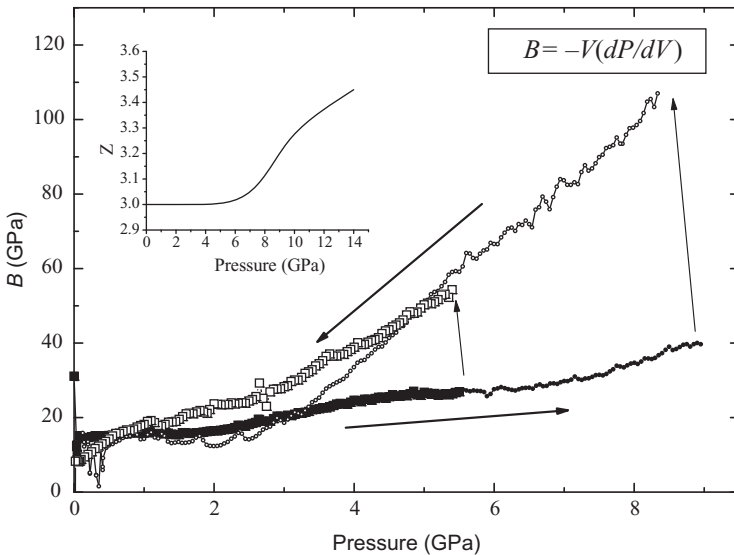


**Figure 6.** Pressure dependencies of the bulk modulus obtained by the direct numerical differentiation of the in situ volumetric measurements of the glassy  $B_2O_3$  under pressure (“relaxed” modulus) in the two different runs of compression (solid symbols) and decompression (open symbols). The significant jumps of the effective bulk modulus between the final of compression and onset of decompression for both runs correspond to the jumps between “relaxed” and almost “unrelaxed” values. The inset shows pressure dependencies of the first coordination number for B from the recent X-ray diffraction data. Both data are from Ref. [129].

intermediate range order; the second transformation is reversible, and it occurs at higher pressures and is accompanied by the change in the coordination of the B atoms from 3 to 4. In  $B_2O_3$  glass, the increased coordination number of cation atoms is not retained at room temperature after decompression either. Similar to silica, the behavior of the glass greatly differs from that of its crystalline counterpart: The  $B_2O_3$  II phase can be retained at normal conditions and has high temperature stability. Ab initio simulations predict one more transition to the glassy state with sixfold coordinated B in the megabar pressure region [129].

Thus, in all discussed oxides, the structural transformations under pressure can be described as a multiple set of transformations. First, changes occur in the intermediate-range order with a slight increase in the coordination number and a transition to the rigid network state; then, a coordination transformation with the increase of the first coordination number follows. According to the computer simulation data, additional buildup of pressure to the megabar range causes a subsequent complementary increase in the coordination number.

It is evident that similar sets of multiple-phase transitions are bound to be observed in the respective melts. Such structural studies on the oxide melts have not yet been carried out, which is because of greater experiment complexity. Nevertheless, the chalcogenide melts, which experience structural transformations at more moderate temperatures and pressures, give examples of multiple phase transitions. Thus, the AsS [29] and CdTe [130] melts feature at least two pressure-induced transitions accompanied by a change in the short-range order structure and properties of the liquids.

### III. WATER

#### A. Preparation of Amorphous Ices

Metastable amorphous solids can in general be prepared from stable phases by bringing in excess free energy [5]. In the case of water, amorphous solids have been prepared from stable phases in all three aggregate states: from the gas, the liquid, and the crystalline solid [131].

##### 1. Preparation from the Gas Phase: Amorphous Solid Water (ASW)

The formation of an amorphous solid was first reported in 1935 [132, 133]. These authors used the route of depositing warm water vapor on a cold substrate, which freezes in excess free energy by the rapid change in temperature. At substrate temperatures above  $\sim 160$  K, the deposit was found to be crystalline ice I, whereas below this temperature, an amorphous solid was obtained. These deposits are referred to as ASW, which is a microporous material that can adsorb gases [134, 135]. In fact, ASW also condenses on interstellar dust particles and is likely the most abundant form of solid water in the universe. Therefore, studies on ASW bear an astrophysical relevance [134, 136]. The microporosity can be reduced greatly by sintering the sample to no more than 120 K.

The density of the ASW films depends highly on the experimental conditions, e.g., on the angle of incidence of the molecular beam. For a deposition temperature of 22 K and at a normal angle, a maximum density of  $0.94 \text{ g/cm}^3$  is observed, whereas a density of  $0.16 \text{ g/cm}^3$  is observed close to glancing incidence, which implies a porosity of 80% [137]. ASW anneals or relaxes during heating in vacuo to a structural state approaching that of hyperquenched glassy water (HW) [138].

Using different deposition rates, even a highly compacted form of amorphous solid water of density  $> 1 \text{ g/cm}^3$  could be obtained at deposition temperature  $T < 30 \text{ K}$ , which transforms gradually in the temperature range 38–68 K to the lower density form of density  $0.94 \text{ g/cm}^3$  [139, 140]. This transition was proposed to be at the origin of crack-formation processes in comets [141]. We note, however, that the formation of this high-density amorph at very low temperatures has been doubted [142, 143]. Only photolysis at 20 K induces a transition to a high-density amorph [143].

## 2. Preparation from the Liquid Phase: HW

Instead of water vapor, also the liquid can be turned into an amorphous solid by cooling. Quenching is a standard method of glass formation for many substances, both organic and inorganic in nature [3, 7]. In fact, it is believed that all liquids can, in principle, be vitrified by cooling. Some liquids can be vitrified easily even by slow cooling (“good glass formers”), whereas others can be vitrified only with difficulties by very rapid cooling (“bad glass formers”). Water is a particularly bad glass former, and a cooling rate of the order of  $10^6$ – $10^7 \text{ K/s}$  is necessary for avoiding crystallization to ice I. Achieving such high cooling rates had required the invention of new techniques, which are called “hyperquenching” or “splat cooling” techniques. Mayer and Brueggeller were the first to succeed by projecting a thin jet of water into a liquid cryomedium [144, 145]. Later, Mayer improved the technique by spraying micrometer-sized droplets on a solid cryoplate, thus avoiding the use of a cryomedium [146]. The droplets are sprayed into a vacuum chamber, which results in the formation of a supersonic jet of droplets. This jet of droplets hits a piece of copper cooled to 77 K, where the droplets are immobilized almost instantaneously. The deposit is called HW.

## 3. Preparation from the Solid Phase

**3.1. High-Density Amorphous Ice (HDA).** When hexagonal ice (ice Ih) is pressurized melting can occur, e.g., at 253 K and 0.2 GPa, because one of water’s anomalies is its negative melting volume, which results in a negatively sloped melting curve according to the Clausius-Clapeyron equation (c.f. Fig. 7). Extrapolating the ice Ih melting curve to lower temperatures, one would expect melting at pressures exceeding  $\sim 1.0 \text{ GPa}$  at 77 K or  $\sim 0.6 \text{ GPa}$  at 170 K if one could avoid recrystallization to high-pressure polymorphs of ice. Whereas at 170 K,

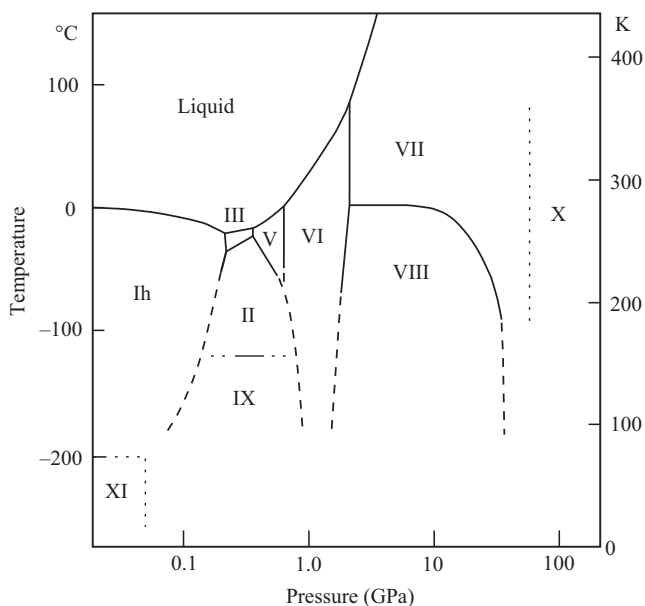


**Figure 7.** Phase diagram of water’s stable crystal polymorphs. Metastable polymorphs such as ice IV or ice XII do not show up. Adapted from Ref. [147].

mixtures of stable ice II and metastable ice III/IX are indeed observed in experiment (c.f. Fig. 7) [148], at 77 K recrystallization is kinetically inhibited. Instead, pressure-induced amorphization takes place, and HDA forms after compressing hexagonal ice [149] or cubic ice [150] beyond 1.1 GPa. It is debated whether this observation can indeed be interpreted as “thermodynamic melting” immediately followed by vitrification of the liquid to the glass (HDA). Alternatively, it was suggested that overpressurization of the crystal results in a collapse of its lattice, i.e., “mechanical melting” producing “nanocrystallites” (see Section III.E) [151]. The density of this amorphous state at 77 K and 1 bar is  $1.17 \text{ g/cm}^3$  [152].

**3.2. Low-Density Amorphous Ice (LDA).** Upon heating HDA to  $T > 115 \text{ K}$  or very high density amorphous ice (VHDA) to  $T > 125 \text{ K}$  at ambient pressure, the structurally distinct amorphous state LDA is produced. Alternatively, LDA can also be produced by decompressing HDA or VHDA in the narrow temperature range of 139–140 K to ambient pressure [153–155]. The density of this amorphous state at 77 K and 1 bar is  $0.93 \text{ g/cm}^3$  [152]. These amorphous–amorphous transitions are discussed in Sections III.C and III.D.

As a third route to LDA, heating or decompression of the high-pressure polymorph ice VIII can be employed, which is the proton-ordered pendant to ice VII. Most high-pressure forms of ice quench-recovered at 77 K experience a

transition to ice Ic when heated above 145–150 K, namely the metastable polymorphs ice IV and ice XII (which can be produced in the stability fields of ice V and ice VI in Fig. 7) [156] and the stable polymorphs ice II, ice III, ice V, ice VI, and ice VII [157, 158]. When ice VIII is heated at 1 bar, temperature-induced amorphization takes place, however [159]. A sequential transformation to first HDA and then LDA was observed when heating ice VIII at 1 bar [160]. Also, the direct route from ice VIII to LDA has been reported: Ice VIII decompressed to 1 bar at 80 K and then heated to 125 K directly transforms to LDA [161]. Also isothermal pathways to LDA by decompression are feasible: By decompressing partially hydrogen ordered ice VII' or ice VIII at 135 K, a transformation directly to LDA is observed using in situ Raman spectroscopy in a diamond anvil cell [162, 163].

Finally, radiation can be employed to produce LDA. Ice III or its proton-ordered counterpart ice IX are amorphized by particle bombardment at electron doses above 2400 electrons  $\text{nm}^{-2}$  [164]. Ice I amorphizes by keV ion-bombardment at 10–80 K [165]. Similarly, after a dose of few eV per mol of UV photons amorphization of ice I is observed [166, 167]. The conversion rates increase as the temperature decreases [168]. Using 700 keV proton irradiation at 13 K, even oscillations between crystalline and amorphous ice can be achieved, whereas above 27 K, the amorphous ice remains [169].

*3.3. Very High Density Amorphous Ice (VHDA).* By annealing HDA to  $T > 160$  K at pressures  $> 0.8$  GPa, a state structurally distinct from HDA can be produced, which is called VHDA ice [152]. The structural change of HDA to a distinct state by pressure annealing was first noticed in 2001 [152]. Even though VHDA was produced in experiments prior to 2001 [170], the structural difference and the density difference of about 10% at 77 K, and 1 bar in comparison with HDA remained unnoticed. Powder X-ray diffraction, flotation, Raman spectroscopy, [152] neutron diffraction [171], and in situ densitometry [172, 173] were employed to show that VHDA is a structural state distinct from HDA. Alternatively, VHDA can be prepared by pressurization of LDA to  $P > 1.1$  GPa at 125 K [173, 174] or by pressure-induced amorphization of hexagonal ice at temperatures  $130 \text{ K} < T < 150 \text{ K}$  [170]. The density of this amorphous state at 77 K and 1 bar is  $1.26 \text{ g/cm}^3$  [152].

## B. Structural Information

Structure factors and radial distribution functions (RDFs) were found to be nearly identical for ASW, HGW, and LDA by X-ray and neutron diffraction measurements [175]. A more recent isotope substitution neutron diffraction study on three sets of samples ( $\text{D}_2\text{O}$ , HDO, and  $\text{H}_2\text{O}$ ) allowed determining the partial OO-, OH-, and HH-radial distribution functions [20]. As an example, the OO-RDF for ASW, HGW, and LDA is shown together with HDA and VHDA in

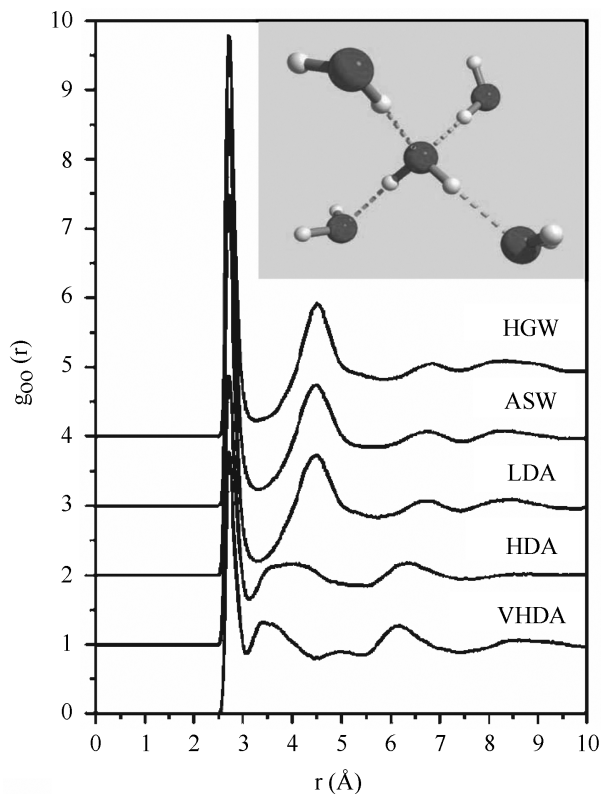


**Figure 8.** The EPSR estimated intermolecular oxygen–oxygen pair distribution function  $g_{OO}(r)$ . For clarity, the functions are offset by a unit. The inset shows the Walrafen pentamer, which is the structural motif common to all known amorphous ices. Adapted from Ref. [20]. See color insert.

Fig. 8. All the partial RDFs for ASW, HGW, and LDA agree within the experimental error, which suggests that ASW, HGW, and LDA all represent the same structural state at 77 K and 1 bar. The basic short-range order structural motif is the “Walrafen pentamer” (i.e., a central oxygen atom, which is surrounded tetrahedrally by four oxygen atoms; c.f. inset Fig. 8.). However, whereas their structures appear identical, it was suggested from inelastic incoherent neutron scattering that the dynamics of lattice and internal vibrations of water molecules differ significantly in HGW and LDA [176].

By contrast, HDA and VHDA differ substantially from ASW, HGW, and LDA in terms of local structure. Most importantly, there is an increased probability of finding water molecules at an OO-distance of 3.0–3.5 Å from the central water molecule. In case of HDA, one molecule is found at an interstitial

position [177], and in the case of VHDA, two molecules occupy the interstitial positions [171]. That is, the coordination number increases from roughly 4 to 5 and 6 for LDA, HDA, and VHDA, respectively.

Information on the nearest-neighbor OO-distances was provided from nuclear magnetic resonance (NMR) measurements at 77 K, which resulted in 2.84 Å for HDA and 2.79 Å for LDA [178]. Raman measurements on H<sub>2</sub>O samples that contain 5 mol% D<sub>2</sub>O can be used to infer near-neighbor OO-distances by calling on a good correlation with the frequency of the decoupled OH stretching band. This correlation suggests OO-distances of 2.85 Å for VHDA, 2.82 Å for HDA, and 2.77 Å for LDA [152]. Thus, increasing density is coupled with increasing OD...O distance. This seemingly paradox situation has been attributed to an increase in coordination number [179].

LDA and HDA were interpreted to be similar to two limiting structural states of supercooled liquid water up to pressures of 0.6 GPa and down to 208 K. In this interpretation, the liquid structure at high pressure is nearly independent of temperature, and it is remarkably similar to the known structure of HDA. At a low pressure, the liquid structure approaches the structure of LDA as temperature decreases [180–182]. The hydrogen bond network in HDA is deformed strongly in a manner analogous to that found in water at high temperatures, whereas the pair correlation function of LDA is closer to that of supercooled water [183]. At ambient conditions, water was suggested to be a mixture of HDA-like and LDA-like states in an approximate proportion 2:3 [184–186].

### C. Irreversible Structural Transitions by Heating at 1 Bar

All amorphous ices transform to cubic ice when heated to  $T > 150$  K at 1 bar, which subsequently recrystallizes to hexagonal ice. However, the high-density amorphous states HDA and VHDA also show an irreversible transition to LDA when heated to temperatures slightly below crystallization. Using ultrasonic sound propagation measurements, three distinct stages were found for the temperature-induced HDA→LDA transformation at 110–115 K, namely shear elastic softening, bulk softening, and main volume jump [187]. Whereas the first stages involve structural relaxation, the final stage is consistent with a “first-order like” transition—that is, the amorphous–amorphous transition shows a complex nonergodic nature that involves more than one process [65]. The relaxation stages of this combined process were studied in detail using neutron scattering [188, 189].

After heating VHDA at 1 bar to ~125–130 K, LDA is produced. There is only one exothermic peak in differential scanning calorimetry (DSC) measurements related to this transition [190]. However, elastic and inelastic neutron scattering experiments performed at narrowly spaced temperatures indicate that an amorphous structure indiscernible from HDA (produced by pressurizing ice Ih at 77 K) forms as an intermediate stage [191]. The small angle scattering indicates that both VHDA and LDA are homogeneous, whereas the intermediate

HDA shows heterogeneities on a length scale of a few nanometers [192]. The activation energy for the VHDA  $\rightarrow$  LDA transition is at least 20 kJ/mol higher than the activation energy for the HDA  $\rightarrow$  LDA transition [191] (i.e., VHDA is thermally more stable at 1 bar than HDA) [170, 190]. Similarly, deuteron spin-lattice relaxation time T1-measurements for the VHDA  $\rightarrow$  LDA transition suggest that an HDA-like state is incurred on the way. The HDA-like state on the way shows a much higher transition temperature to LDA than HDA (produced by pressurizing ice Ih at 77 K), which suggests that it is in a relaxed HDA state [193]. Mishima and Suzuki have performed Raman measurements on a VHDA sample and have monitored the transition to LDA as a function of temperature, time, and position on the amorphous sample [194]. In Fig. 9, it is shown that the measured VHDA Raman peak shift and intensity as well as the estimated sample density first continuously change toward HDA in the temperature range 100–115 K and then discontinuously change (marked by the arrows in Fig. 9) at  $\sim$  116 K. Mishima and Suzuki [194] noticed that in the course of the transition, a “phase” boundary propagates through the sample. These results confirm a picture of a combined process that first involves structural relaxation at 1 bar followed by a “first-order like” transition that involves HDA-LDA coexistence. Please note, however, that these transitions are irreversible in the sense that going back to 77 K, the back transformation to HDA or VHDA, cannot be achieved. Thus, equality of Gibbs free energies is not involved in this case—rather, LDA has a much lower Gibbs free energy at 1 bar than HDA or VHDA.

#### D. Reversible in situ Structural Transitions

By contrast, after changing the pressure, a reversible transition is observed. The upstroke transition from LDA to HDA was first observed by noticing a sharp 20% volume change at 0.55–0.65 GPa and 77 K, which causes a shift in the halo peak of the powder X-ray diffractogram of the quench-recovered state [25]. At higher temperatures, the sharp LDA  $\rightarrow$  HDA transition shifts to lower pressures [153] (e.g., to 0.40–0.50 GPa at 125 K) [174]. Whereas HDA can be quench recovered at 77 K without structural change, it transforms back to LDA on the downstroke between 130 K and 140 K [153]. Under strictly isothermal conditions, the sharp downstroke transition is observable solely in a narrow temperature region. The transition is observed at 139 K and  $\sim$  0.03 GPa [154] and at 140 K and  $\sim$  0.06 GPa [155], whereas no such transition is observed at 136 K. Instead, HDA is recovered after decompressing to ambient pressure at 136 K. At 142 K, crystallization of HDA to an ice IX/ice V mixture is observed rather than the downstroke HDA  $\rightarrow$  LDA transition. An observation of the HDA  $\rightarrow$  LDA transition at temperatures  $T < 136$  K would require negative pressure (i.e., a substantial hysteresis is involved).

When pressurizing LDA and by monitoring the structural state using in situ neutron diffraction, double-peaked diffraction patterns and a progressing

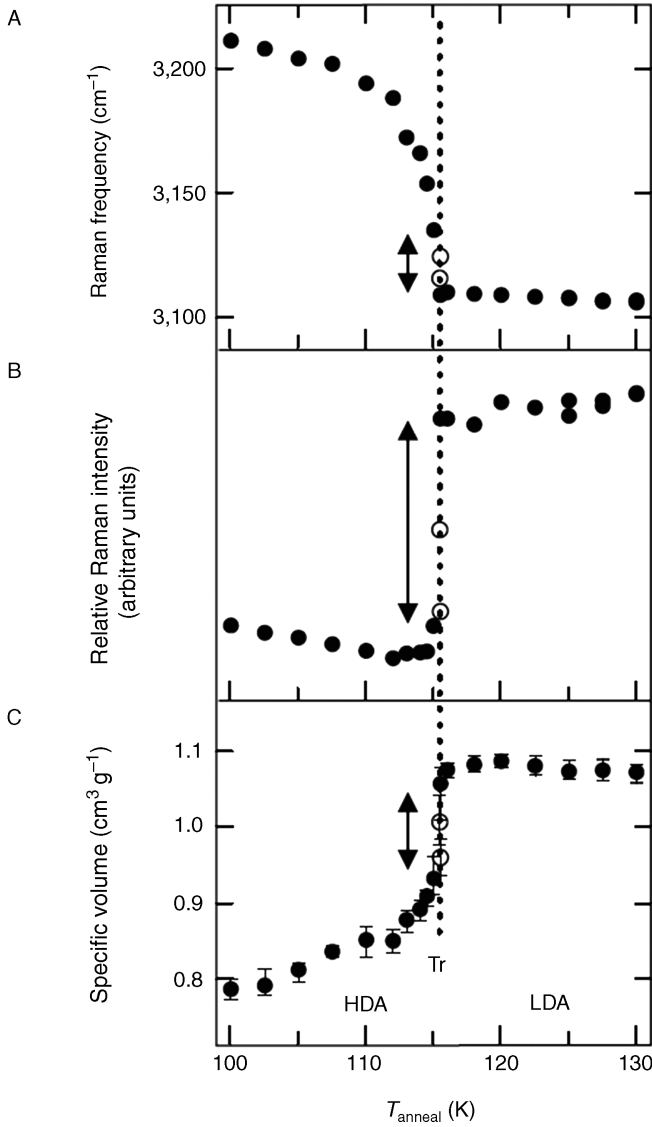


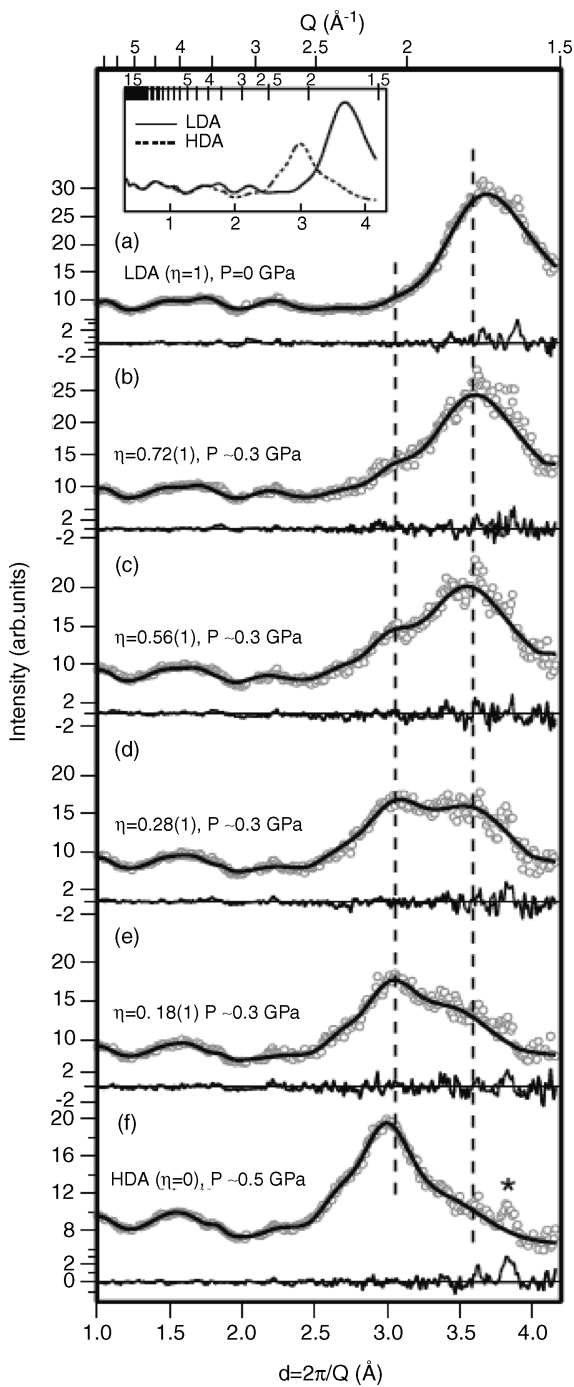
**Figure 9.** Changes in properties of VHDA ice induced by annealing at 1 bar. Up to 115 K continuous changes toward HDA can be observed. The discontinuous changes at the transformation at  $\sim 116$  K are marked by gaps/arrows. Raman spectra can all be expressed as a superposition of pure LDA and pure HDA spectra. The specific volume in the bottom panel is estimated from visual inspection of the sample expansion. Reproduced from Ref. [193].

transformation to HDA were observed at  $\sim 0.3$  GPa and 130 K [195]. The intermediate double-peaked patterns shown in Fig. 10, panels (b)–(e), can be decomposed into a linear combination of the patterns of pure LDA and HDA, which suggests coexistence of the two amorphs. A progressive transformation from one state (LDA) to another state (HDA) is consistent with the data obtained during pressurization and is suggested by the authors to be evidence for a “classic first-order,” transition. Please note, however, that there is an inherent nonequilibrium character to amorphous–amorphous transitions, because amorphous states by definition structurally relax on the time-scale of the experiment. This structural relaxation, even though it is very slow and so small that it cannot be resolved within their experimental setup, is superimposed on the first-order transition. Therefore, we prefer the notion of a “first-order like,” a “quasi first-order,” or an “apparently first-order” transition, which was first used by Mishima et al. [25]. We also note that the conclusion of coexistence was doubted, and the occurrence of intermediate amorphous ices was suggested because (1) neutrons rather than X-rays were employed, (2) pressure gradients may blur the analysis, and (3) a peak shift parameter was necessary in the fit procedure [197].

We now turn from the single, possibly “first-order like” nature of the LDA–HDA transition to the multiple amorphous–amorphous transitions in water. When pressurizing LDA at slow rates at 125 K, a stepwise transition LDA  $\rightarrow$  HDA  $\rightarrow$  VHDA is observed [173]. The piston displacement and density data as obtained from a piston-cylinder experiment that shows the stepwise nature are depicted in Fig. 11. The upstroke HDA  $\rightarrow$  VHDA densification of 5% takes place in the pressure range 0.80–0.95 GPa and is somewhat less sharp when comparing with the upstroke LDA  $\rightarrow$  HDA densification of 20% at 0.40–0.50 GPa. During fast compression, the LDA  $\rightarrow$  HDA transition is still sharp, whereas the HDA  $\rightarrow$  VHDA transition is smeared out over a broad pressure range [173]. These findings support the possibility of an LDA–HDA first-order like transition but leave the question open whether a first-order like transition underlies the HDA  $\rightarrow$  VHDA transition and/or whether the observed second step

---

**Figure 10.** Neutron diffraction patterns as LDA (top,  $\eta = 1$ ) transforms to HDA (bottom,  $\eta = 0$ ) at 130 K. The measured data are shown using open circles. Parameterizations to the data are shown using lines. Parameterizations of pure LDA at 0 GPa [panel (a)] and pure HDA at 0.5 GPa [panel (f)] are shown in the inset. The measured data on the upstroke transition at a roughly estimated pressure of  $\sim 0.3$  GPa [panels (b)–(e)] can be fitted to linear combinations of pure LDA and pure HDA patterns, where  $\eta$  indicates the fraction of LDA in the binary LDA–HDA mixture. Peak shift parameters were employed to account for the peak shift incurred by bringing LDA from 0.0 GPa to 0.3 GPa and HDA from 0.5 GPa to 0.3 GPa. The subtraction of the fitted data from the measured data is shown below each pattern. The asterisk in panel (f) marks a peak of a small amount of untransformed hexagonal ice. The amount of the ice contamination remains constant during the whole experiment because the amorphization of hexagonal ice at 130 K requires pressures much higher than 0.5 GPa [174, 196]. Reproduced from Ref. [195].



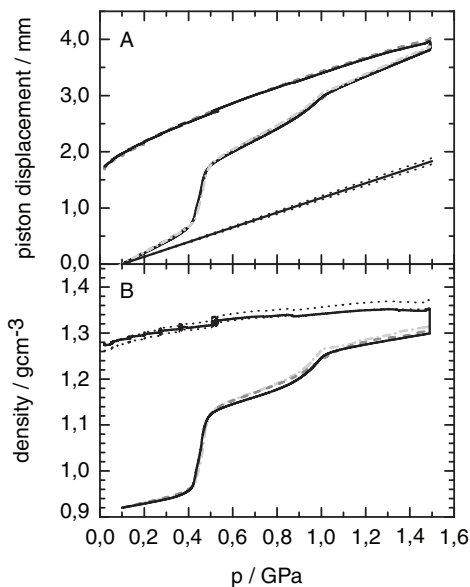


**Figure 11.** (a) Three curves of “raw” piston displacement data obtained on compressing 300 mg of LDA at 125 K in a piston-cylinder apparatus with a bore diameter of 8 mm at a rate of 20 MPa/min, quenching to 77 K at 1.5 GPa and subsequent pressure release at 77 K (top curves) together with the apparatus correction (straight line at bottom). (b) Density data calculated from the “raw” piston displacement curve and the apparatus correction with the use of Eq. (1) given in Ref. [174]. Adapted from Ref. [174].

is caused by a slow relaxation of HDA to the metastable equilibrium state at 125 K. One way of answering this question is by accelerating the relaxation dynamics by working at higher temperatures (i.e., by working as close as possible to the metastable equilibrium). The highest possible temperature at which crystallization does not interfere is 140 K in case of the downstroke transition [154]. When decompressing VHDA at 140 K, a single density step is observed at  $\sim 0.06$  GPa, which is caused by the HDA  $\rightarrow$  LDA downstroke transition [154]. No density step is related to the VHDA  $\rightarrow$  HDA transition. Whereas the structural state of VHDA does not change in the pressure range from 1.1 GPa down to  $\sim 0.4$  GPa, a continuous structural transition to HDA is observed in the range from  $\sim 0.40$  GPa down to  $\sim 0.06$  GPa. The corresponding X-ray diffractograms are shown in Fig. 12 [panel (a)] together with an analysis of the peak position [panel (b)] and full width at half maximum [panel (c)] for the first broad diffraction peak. Many intermediate states exist between HDA and VHDA, which can be quench-recovered, whereas no intermediate states can be quench-recovered between LDA and HDA. The HDA state quench-recovered at 0.7 GPa in the upstroke transition at 125 K (cf. Fig. 11) resembles state

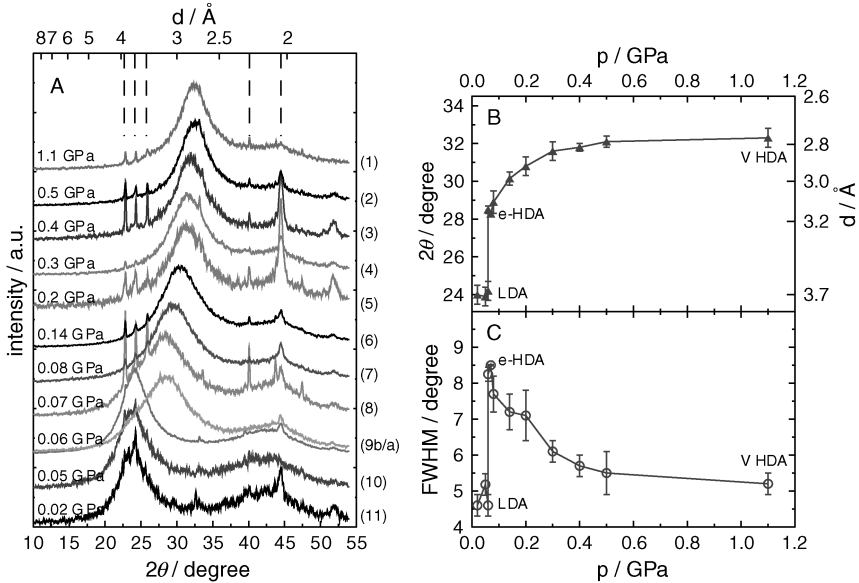


**Figure 12.** (a) Powder X-ray diffractograms obtained by isothermal decomposition of VHDA (sample 1) at 140 K to several selected pressures, subsequent quenching to 77 K and recovery to ambient pressure (samples 2–11). The diffractograms (Cu  $K\alpha$ ) were recorded at  $\sim 83$  K on a diffractometer in  $\Theta$ – $\Theta$  geometry (Siemens, New York, NY; model D 5000), equipped with a low-temperature camera of Anton Paar. Curves are shown on the same scale and smoothed with a 21-point Savitzky-Golay polynomial of fifth order. Data are offset and scaled for clarity. The right panel shows (b) the peak position and (c) the full width at half maximum (FWHM) of the first broad diffraction peak as a function of the selected decomposition pressure. For part (b), the experimental error of a single measurement is  $\pm 0.5^\circ$ . In some powder diffractograms, sharp features marked by the dashed lines can be observed. They develop from traces of  $I_h$ , which had formed by condensation of water vapor during transfer of the sample onto the precooled sample holder [198], the X-ray sample holder itself (chrome-plated Cu:  $2\theta = 44.5^\circ$ ), or remnants of indium. The samples themselves are fully amorphous. Reproduced from Ref. [155].

number 6 in Fig. 12, which was quench-recovered on the downstroke transition from 140 K and 0.14 GPa. The occurrence of intermediate states is evidence that no first-order character underlies the HDA  $\leftrightarrow$  VHDA transition, even though both the upstroke and the downstroke transition take place in a narrow pressure interval. We note that the HDA, which transforms to LDA in a first-order-like manner, is a structural state distinct from the HDA, which is produced by pressure-induced amorphization of hexagonal ice at 77 K, because the latter is unrelaxed and far away from the metastable equilibrium state, whereas the former is structurally relaxed and much closer to the metastable equilibrium. Nelmes et al. [199], therefore, suggested distinguishing the two states by calling the latter “unrelaxed HDA” (uHDA) and the former “expanded HDA” (eHDA).

The density of eHDA is  $1.13 \text{ g/cm}^3$ , which is about 4% less than the density of uHDA [200]. The different degree of structural relaxation should be evident when studying the thermal stability at 1 bar. The well-relaxed state is expected to be thermally more stable, and this expectation is confirmed experimentally: At 1 bar, eHDA is stable up to  $\sim 135 \text{ K}$ , whereas uHDA is stable merely up to  $\sim 115 \text{ K}$  [190, 194, 196]. Earlier, Johari [201] had noticed that HDA produced from LDA (“eHDA”) shows ultrasonic properties that differ from HDA produced from ice Ih (“uHDA”).

A summary in the form of a “diagram of metastable amorphous states” is depicted in Fig. 13, in which the upstroke–downstroke hysteresis has been averaged out. The vertical arrow represents the pressure annealing from

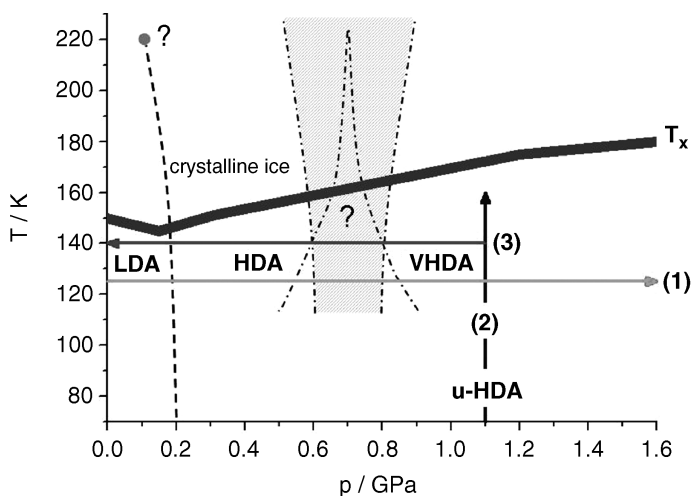


**Figure 13.** Schematic phase diagram of water’s metastable states. Line (1) indicates the upstroke transition  $\text{LDA} \rightarrow \text{HDA} \rightarrow \text{VHDA}$  discussed in Refs. [173, 174]. Line (2) indicates the standard preparation procedure of VHDA (annealing of uHDA to 160 K at 1.1 GPa) as discussed in Ref. [152]. Line (3) indicates the reverse downstroke transition  $\text{VHDA} \rightarrow \text{HDA} \rightarrow \text{LDA}$  as discussed in Ref. [155]. The thick gray line marked  $T_x$  represents the crystallization temperature above which rapid crystallization is observed (adapted from Mishima [153]). The metastability fields for LDA and HDA are delineated by a sharp line, which is the possible extension of a first-order liquid–liquid transition ending in a hypothesized second critical point. The metastability fields for HDA and VHDA are delineated by a broad area, which may either become broader (according to the singularity free scenario [202, 203]) or alternatively become more narrow (in case the transition is limited by kinetics) as the temperature is increased. The question marks indicate that the extrapolation of the abrupt  $\text{LDA} \leftrightarrow \text{HDA}$  and the smeared  $\text{HDA} \leftrightarrow \text{VHDA}$  transitions at 140 K to higher temperatures are speculative. For simplicity, we average out the hysteresis effect observed during upstroke and downstroke transitions as previously done by Mishima [153], which results in a  $\text{HDA} \leftrightarrow \text{VHDA}$  transition at  $T = 140 \text{ K}$  and  $P \sim 0.70 \text{ GPa}$ , which is  $\sim 0.25 \text{ GPa}$  broad and a  $\text{LDA} \leftrightarrow \text{HDA}$  transition at  $T = 140 \text{ K}$  and  $P \sim 0.20 \text{ GPa}$ , which is at most  $0.01 \text{ GPa}$  broad (i.e., discontinuous) within the experimental resolution.

unrelaxed HDA (produced at 77 K from ice Ih) at 1.1 GPa to 160 K to VHDA. VHDA represents the ultimately densified amorphous state of water, which crystallizes rather than densifies when compressed beyond 2 GPa [204]. The left-facing arrow shows the downstroke transition at 140 K. VHDA gradually transforms to HDA in a finite pressure interval. To distinguish this relaxed form of HDA from uHDA, the term “expanded HDA” is preferable. eHDA represents the ultimately expanded state of HDA, which transforms to LDA possibly in a first-order like transition and which may coexist with LDA. Such a coexistence has been inferred for the upstroke transition [195]. Continued compression of HDA along the right-facing arrow results in a second transition to VHDA, which is continuous but confined to a finite pressure interval. Both eHDA and VHDA are well relaxed and at least close to being metastable equilibrium states. uHDA, however, is an unstable state and inevitably relaxes structurally during heating. As a working hypothesis, one can assume that eHDA is the closest possible amorphous state directly related to a deeply supercooled high-density liquid on the low pressure side (e.g., at 0.2 GPa) and that VHDA is the closest possible proxy of a deeply supercooled very high-density liquid on the high-pressure side (e.g., at 1.5 GPa). In addition, there is a possible low-density liquid related to LDA, and hence, there may be three deeply supercooled liquids. A direct experimental proof for such a correspondence between amorphous states and deeply supercooled liquids is missing currently. What needs to be done here is to measure the in situ relaxation times directly and to determine whether a glass→liquid transition occurs during isobaric heating. The first results obtained by dielectric relaxation spectroscopy of VHDA at 1 GPa suggest that VHDA indeed shows liquid-like relaxation behavior at 140 K [205, 206]. The question of whether the amorphous states of water behave like glasses (i.e., vitrified liquids), which turn into liquids during heating, or whether they behave like crystals, which do not liquify during heating, is highly disputed as outlined in the following section.

### **E. Are the Amorphous Solids Glasses or Nanocrystallites?**

The question of whether there is a true glassy nature of amorphous ices is of interest when speculating about possible liquid–liquid transitions in (deeply) supercooled water. For true glasses, the amorphous–amorphous transitions described here can be viewed as the low-temperature extension of liquid–liquid transitions among LDL, HDL, and possibly VHDL. That is, the first-order like LDA ↔ HDA transition may map into a first-order LDL ↔ HDL transition, and the continuous HDA ↔ VHDA transition may map into a smeared HDL ↔ VHDL transition. Many possible scenarios are used how to explain water’s anomalies [40], which share the feature of a liquid–liquid transition [202, 207–212]. They differ, however, in the details of the nature of the liquid–liquid transition: Is it continuous or discontinuous? Does it end in a liquid–liquid critical point or at the reentrant gas–liquid spinodal?

Except for HGW, which is commonly accepted to be a true glass, there is a lot of debate and scientific discourse regarding a possible nanocrystalline nature of amorphous ices. Evidence is abundant in the literature both for a “pro-glass” and a “contra-glass” view.

In the case of LDA, it has been suggested that it behaves in many respects similar to ice I. Comparison of vibrational spectra and oxygen *K*-edge X-ray absorption spectra of LDA with ice [151, 213, 214] and an analysis of Gibbs free energies (which indicates that LDA would need to transform to ice Ih by pressurizing to 0.7 GPa at 77 K rather than HDA if LDA were indeed a glass) suggest that LDA is not a truly amorphous material [215]. The absence of fast precursor dynamics in LDA during heating from 2 K to 170 K in elastic high-*Q* backscattering neutron diffraction was interpreted as evidence against the glassy nature of LDA, because fast precursor dynamics would be expected from predictions by mode coupling theory near the glass transition [216]. Inelastic X-ray scattering in the 1–15 nm<sup>-1</sup> momentum transfer (*Q*) range shows sharp, crystal-like phonons [217]. Also, crystal-like features in the thermal conductivity of LDA indicate that phonon–phonon scattering is dominant [218]. LDA, like cubic ice and hexagonal ice, shows a negative Bridgman parameter, which characterizes the density dependence of the thermal conductivity. However, the 1H-spin lattice relaxation time of LDA (and also HDA) at 77 K is very different from the 1H-spin lattice relaxation time of crystalline ices [178]. Also, a thermally reversible glass→liquid transition was measured in LDA at a temperature of 134 K, which is accompanied by a change in heat capacity  $\Delta c_p \sim 0.7$  J/Kmol [219]. (Please note that  $T_g$  for LDA was initially erroneously reported to be 129 K [220–222]). The DSC curves for LDA are remarkably similar to the DSC curves of annealed ASW [138] and HGW [223–226], which both show a  $T_g$  of 136 K at a heating rate of 30 K/min. The activation energy of structural relaxation near  $T_g$  was determined to be  $\sim 55$  kJ/mol [224]. So, judging from DSC experiments, HGW, ASW, and LDA are very similar not only in terms of static structure as outlined in Section III.B, but also in terms of their glass→liquid transition [138, 219]. Ultrafast scanning of pure ASW samples at a heating rate of up to 10<sup>5</sup> K/s seems to be in contradiction, because no sign of a glass→liquid transition up to  $\sim 205$  K was reported, where it crystallizes to ice Ic [227]. However, Johari [228] suggested that this conclusion was made prematurely, and a reanalysis of the data is necessary. To resolve the question of whether a difference exists between LDA, which may be nanocrystalline or a glass, and HGW, which is definitely a glass, it would be highly instructive to study vibrational spectra and thermal conductivity in HGW samples and compare the results directly with the LDA case.

In the case of ASW, the self-diffusivity shows contradicting experimental evidence. At temperatures up to 125 K, the mobility of protons injected into annealed D<sub>2</sub>O-ASW at 80 K was shown to be consistent with orientational

diffusion based on L-defect activity rather than molecular diffusion. This finding suggests that fluidity does not develop when heating to above the glass→liquid transition at 136 K and that the isotopic exchange behavior in annealed D<sub>2</sub>O-ASW resembles the behavior in cubic ice [229]. However, the self-diffusivity as measured by hydrogen/deuterium (H/D) isotope exchange in the 150–160 K range is roughly a millionfold greater than that expected for crystalline ice and is in accordance with a fluid-like translational diffusive motion. This is consistent with an amorphous solid that melts into a deeply supercooled liquid prior to crystallization [230, 231]. Self-diffusivity measurements performed by thermal desorption spectroscopy in layered films of ASW and organic spacers indicate that interlayer mixing in the 150–160 K range does not occur by diffusion through a dense phase but through an interconnected network of cracks/fractures created within the ASW film during crystallization. This implies that the self-diffusivity of ASW below crystallization is inconsistent with a “fragile” liquid and leaves the two options of (1)  $T_g > 160$  K or (2) the liquid above  $T_g \sim 136$  K is a “strong” liquid [232, 233]. The picture of ASW transforming into a “strong” liquid above  $T_g \sim 136$  K is supported by electron diffraction studies of the crystallization behavior of ASW. These studies show an onset of the amorphous relaxation (coincident with the glass transition) *prior* to crystallization. Above the glass transition temperature, the crystallization kinetics, film morphology changes, changes in binding energy of water molecules, and band shape changes are consistent with the amorphous solid becoming a “strong” ultraviscous liquid [234, 235]. The concept of a dynamic crossover from “fragile” (at  $T > 230$  K) to “strong” (at  $T < 150$  K) was also invoked for the case of HGW. Although it was suggested initially that the weak glass→liquid transition in HGW at  $\sim 136$  K [222] would merely be a shadow of a pronounced but hidden glass→liquid transition at  $\sim 160$ – $165$  K [236, 237], the consensus is now that the weak endothermic step observed at  $\sim 136$  K is a real glass→liquid transition to a deeply supercooled “strong” liquid [212, 225, 226, 238].

In the case of HDA, it has been proposed that HDA may be a mixture of highly strained nanocrystalline high-pressure phases of ice instead of being a homogeneously random structure [239]. Also for VHDA, it was suggested [240] that its structure factor is highly reminiscent of the structure factor obtained for a mechanically collapsed and densified ice [241]. From inelastic neutron scattering, it was inferred that HDA shows vibrational spectra similar to ice VI [242], (i.e., short-range atomic correlations and force constants are similar in HDA and ice VI, whereas the degree of disorder on a long-range scale differs). Inelastic neutron scattering (INS) shows that the first phonon peak in the 0.5–20 meV range is softer for LDA compared with HDA [243]. However, INS in the energy transfer region 2–500 meV (i.e.,  $16$ – $4025$  cm<sup>-1</sup>) shows HDA to behave glass-like in the translational and librational regions ( $< 150$  meV) [214]. Other INS studies illustrate clearly an excess number of modes in the HDA density of states at 5 K

centered at 0.65 THz, which is not found in LDA, ice Ic, or ice Ih [244]. The thermal conductivity of HDA ice under pressure, by contrast to LDA, follows the behavior expected for a glass and a positive Bridgman parameter [218]. Similarly, the Gruneisen parameter that characterizes low-frequency phonons is negative for LDA (i.e., crystal like), but is positive for HDA (i.e., glass like) [245]. Also, the two-level system density of states in HDA is comparable with that found in many conventional glasses (by contrast to LDA) [246].

The phonon dispersion of hexagonal ice measured by inelastic neutron scattering up to 0.5 GPa at 140 K reveals a pronounced softening (e.g., for a transverse acoustic phonon branch), which is suggested to be at the origin of anomalous features of hexagonal ice, such as its negative thermal expansion coefficient below 60 K and solid-state amorphization [247]. Extrapolation of the data to 2.5 GPa, where some mode frequencies approach zero, suggests that pressure-induced amorphization of hexagonal ice is caused by mechanical melting rather than by thermodynamic melting. An ultrasonic study suggests that the ice Ih  $\rightarrow$  HDA transition is, very much alike the LDA  $\rightarrow$  HDA transition, preceded by elastic softening. This finding can be interpreted in favor of the crystal lattice instability paradigm [187, 248]. Whereas at low temperatures ( $< 162$  K), the Born stability criterion of lattices is violated (“mechanical melting”), at higher temperatures ( $> 162$  K) a Lindemann transition is observed (“thermodynamic melting”) [151, 249]. It has been noted that the mechanism of solid-state amorphization is not only temperature dependent but also time- and pressure-dependent, and it cannot be described in terms of Born/Lindemann criteria as long as crystal-size effects (stresses at grain boundaries, etc.) and production of lattice faults during uniaxial pressurization are incorporated properly [239, 250].

The best evidence so far for the glassy nature of HDA was provided (1) by measurements of the dielectric relaxation time under pressure at 140 K [206, 251], (2) by the direct vitrification of a pressurized liquid water emulsion to HDA [252], and (3) by a high-pressure study of the glass  $\rightarrow$  liquid transition using differential thermal analysis (DTA) [253]. We note here that these studies probe structurally relaxed HDA (eHDA) rather than unrelaxed HDA. It is possible that structurally relaxed HDA behaves glass like, whereas structurally uHDA shows a distinct behavior. Thus, more studies are needed in the future, which directly compare structurally relaxed and unrelaxed HDA.

## IV. SEMICONDUCTORS

### A. General Comments

The tetrahedral open network is a specific characteristic not only of water and silica but also of covalent systems such as Si and Ge (group IV semiconductors) [254, 255]. These substances share many characteristics with water, such as

locally tetrahedral coordination at ambient pressure, negative melting slope in the P-T phase diagram, denser liquid than its crystalline form, and so on. All of these characteristics come from the tetrahedral network structure, which in fact plays a key role in water's polyamorphism. Because the tetrahedral network in Si and Ge is preserved in amorphous forms as well as in crystalline forms at ambient pressure, one naturally expects that Si and Ge exhibit polyamorphic transformations similar to those in water (ice).

Unlike that in water, the tetrahedral network in Si and Ge mainly consists of covalent interatomic bonding, which makes the network more rigid than hydrogen bonding, leading to relatively high melting temperatures (e.g., 1687 K for *c*-Si). Although crystalline and amorphous states at ambient pressure hold the rigid network that exhibits a semiconducting nature, liquid and solid states under high pressure contain a highly distorted or collapsed tetrahedral network, which results in a metallic nature. The semiconductor–metal transition would thus be likely to accompany polyamorphic transformations in Si and Ge, in contrast to those in water. Because of such a substantial change in the electronic state (interatomic bonding), a two-state model [256–259] has often been invoked to describe polyamorphic transformations in Si and Ge. This model was originally developed by Rapoport [256] to account for the anomalous (negative) slope of the melting curve in tetrahedrally coordinated liquids.

## B. Amorphous Si

Convincing evidence for multiple amorphous phases in Si has been provided only recently. The first indication of pressure-induced amorphous–amorphous transition in Si was reported by Shimomura and colleagues [260, 261]. The electronic resistance of an amorphous Si (*a*-Si) film of about 1  $\mu\text{m}$  thickness was measured in a compression–decompression cycle [260]. The electronic resistance showed a substantial drop at about 10 GPa in the compression process, which indicates a transition to a metallic state. In the decompression process, in contrast, the electronic resistance showed a large hysteresis and returned to the original semiconducting value only gradually. X-ray diffraction patterns were measured at 0 GPa for both the initial and final samples in the compression–decompression cycle, and amorphous patterns were obtained for both samples [260]. However, the X-ray diffraction patterns were not obtained for the metallic sample under pressure, so it remains uncertain whether densified metallic Si retained an amorphous form at  $\sim 10$  GPa. In fact, other experiments have shown that *a*-Si is transformed to  $\beta$ -tin crystal (a high-pressure polymorph [255]) above 10 GPa [262], which may have been realized in the experiment of Shimomura et al. [260].

Instead of pressurizing *a*-Si, Deb et al. [263] obtained a densified *a*-Si via pressurizing porous Si. They prepared films of porous Si having crystallite of  $\sim 5$  nm (on average). In situ measurements of X-ray diffraction patterns and

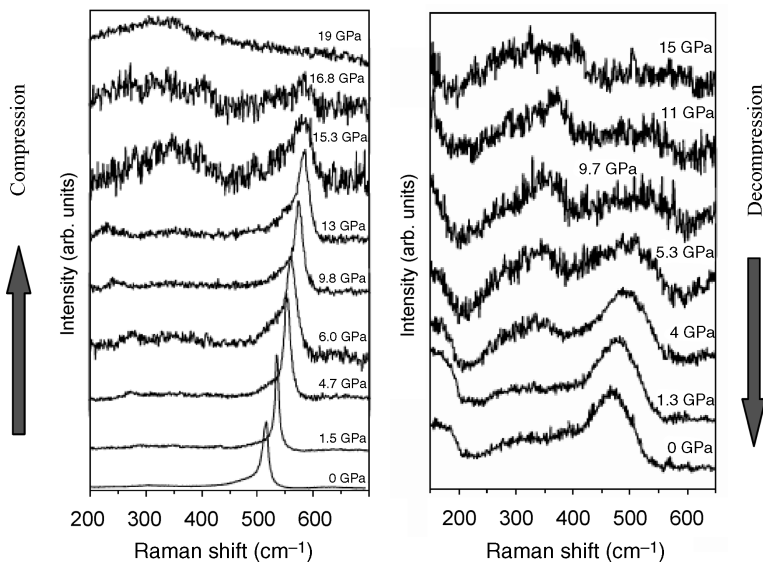


**Figure 14.** Raman spectra of porous Si in a compression–decompression cycle [263]. In the compression process, the characteristic spectrum of nanocrystalline Si disappears above  $\sim 13$  GPa and a broad amorphous feature emerges. In the decompression process, the characteristic spectrum of the LDA form grows below  $\sim 9$  GPa, which indicates an HDA-to-LDA transition.

Raman spectra for the sample were conducted in a compression–decompression cycle. In this experiment, the crystalline diffraction began to disappear above 7–8 GPa during compression, and pressure-induced amorphization was indicated by the Raman spectra above  $\sim 13$  GPa (Fig. 14). The resultant HDA Si exhibits the Raman spectrum that differs from the spectrum of normal  $\alpha$ -Si (LDA Si). Rather, the characteristics of the spectrum for HDA Si resemble those of the  $\beta$ -tin crystal, which indicates that HDA Si has a (locally) analogous structure to the  $\beta$ -tin structure. The synthesis of the HDA form of Si by Deb et al. [263] has a strong resemblance to that of water (ice) by Mishima et al. [149, 196]. Whereas compression induced amorphization that was almost completed at 13–15 GPa, decompression induced an HDA–LDA transition below 10 GPa, which is clearly shown in the Raman spectra (Fig. 14). This is the first direct observation of an amorphous–amorphous transition in Si. The spectrum at 0 GPa after the pressure release exhibits the characteristic bands of tetrahedrally coordinated  $\alpha$ -Si (LDA Si). Based on their experimental findings Deb et al. [263] discussed the possible existence of liquid–liquid transition in Si by invoking a bond-excitation model [258, 259]. They have predicted a first-order transition between high-density liquid (HDL) and low-density liquid

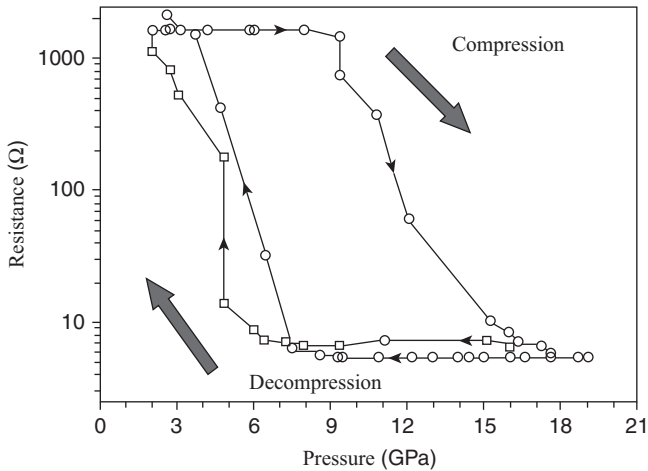


**Figure 15.** Electrical resistance measurements of a-Si in a compression–decompression cycle [264].

(LDL) below 1600 K at 1 atm and a second critical point at a negative pressure [263].

The transition from LDA to HDA Si was observed in the successive experiment by McMillan et al. [264]. In situ Raman spectra and electronic resistance measurements were performed with optical observation. After compression, the LDA form prepared by solid-state metathesis synthesis [10] was found to be transformed to the HDA form at  $\sim 14$  GPa. The electronic resistance exhibited a sharp decrease at 10–14 GPa (Fig. 15), which is consistent with the early experimental findings by Shimomura et al. [260]. Optical micrographs show that HDA Si is highly reflective, whereas LDA Si is dark colored and nonreflective. This finding again supports that the LDA–HDA transition of Si is accompanied by a semiconductor–metal transition. Reverse transitions with large hysteresis were also observed; LDA Si began to form from HDA Si at 4–6 GPa after decompression from  $\sim 20$  GPa.

It should be noted that no direct structural information about HDA Si was obtained in the experiments by Deb et al. [263] and McMillan et al. [264]. Their experimental data imply that HDA Si is structurally based on the  $\beta$ -tin structure, but the data are not sufficient to experimentally determine the structure of HDA Si.

Computer simulation studies have taken the lead in disclosing structural properties of HDA Si. In particular, *ab initio* calculations are playing a significant role in predicting the structural properties of HDA Si [265, 266]. *Ab initio* molecular-dynamics (MD) simulations based on plane-wave density functional theory (DFT) were performed by Morishita [265] to investigate the

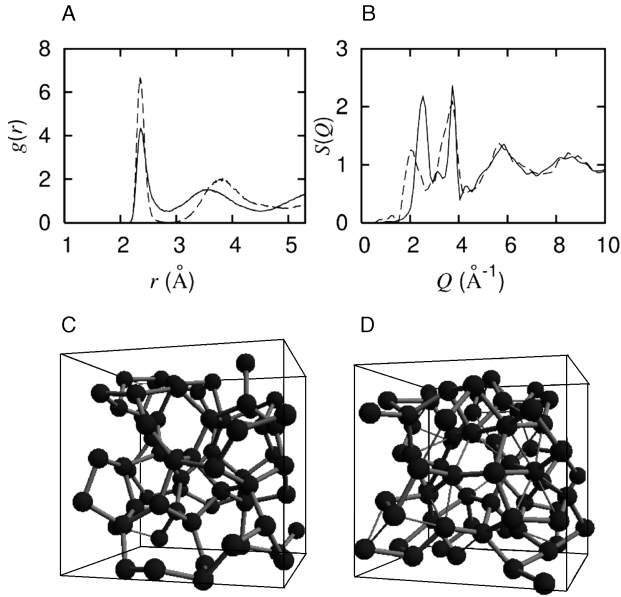


**Figure 16.** Structural profiles of LDA and HDA Si obtained from the plane-wave DFT calculations [265]. (a) Pair correlation functions  $g(r)$  for HDA (at 12 GPa, solid lines) and LDA (at 0 GPa, dashed lines). (b) Structure factors  $S(Q)$  for HDA (at 12 GPa, solid lines) and LDA (at 0 GPa, dashed lines). (c, d) Atomic configurations for (c) LDA and (d) HDA. Atoms separated by 2.55 Å or less are linked by thick lines (covalent-like bonds), whereas those separated by 2.857 Å or less are linked by thin lines.

LDA–HDA transition of Si at an atomistic level. LDA Si was pressurized in a stepwise manner, whereas the temperature was maintained at 300 K. At 12 GPa, the LDA form was transformed to the HDA form with large volume reduction ( $\sim 10\%$ ). The pair correlation functions  $g(r)$  for the LDA form and the HDA form thus obtained are given in Fig. 16. The first peak of  $g(r)$  is considerably broadened and becomes less intense after the transition to HDA. The second peak shifts to smaller  $r$ , and the separation between the first and second peaks is not as clear in HDA as in LDA. The coordination number  $N_c$  obtained by integrating  $4\pi r^2 \rho^* g(r)$  up to the first minimum is 4.0 for LDA, whereas it is 5.1 for HDA (where  $\rho^*$  is the number density). Detailed structural analyses indicate that the first four neighboring atoms in HDA still form a (distorted) tetrahedral configuration, but the fifth neighboring atom is located at an open space of the tetrahedron (Fig. 16). It is thus considered that the HDA structure is constructed by forcing the fifth neighboring atom, which is outside of the first coordination shell of the LDA structure, into an interstitial position. This mechanism

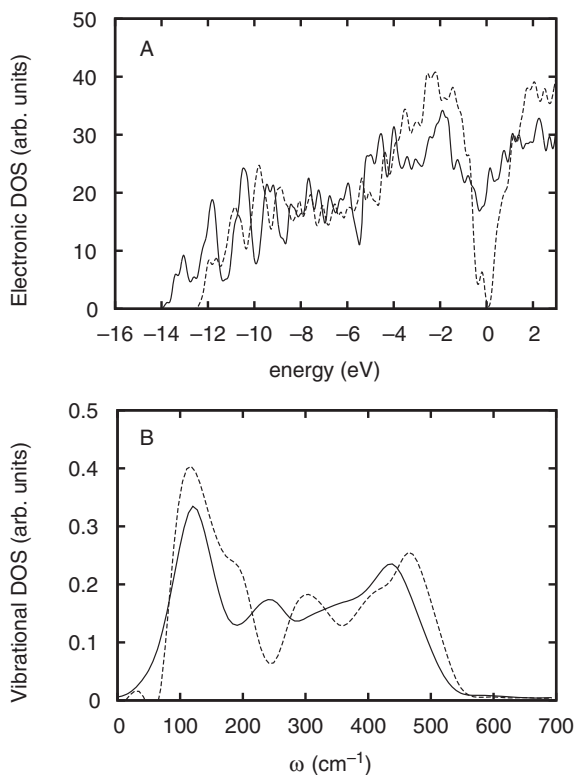


**Figure 17.** (a) EDOS for HDA (solid lines) and LDA (dashed lines). The Fermi energy is set to 0 eV. (b) VDOS for HDA (solid lines) and LDA (dashed lines). Both EDOS and VDOS were obtained from the plane-wave DFT calculations.

resembles the formation mechanism of the HDA ice structure [177], which indicates an inherent nature of tetrahedrally coordinated materials under pressure.

The electronic densities of states (EDOS) calculated for LDA and HDA Si (Fig. 17) confirm that HDA is metallic, as suggested by the experimental results [264]. There is no gap at the Fermi energy in EDOS for HDA, as Fig. 17 shows clearly. The calculated vibrational densities of states (VDOS) are also consistent with the previous experimental results [263, 264]. The LA and LO bands ( $\sim 300$  and  $\sim 420$   $\text{cm}^{-1}$ , respectively) in LDA are broadened, and the TO band ( $\sim 500$   $\text{cm}^{-1}$ ) shifts to a lower frequency after the transition to HDA. This results in broad intensity in the range 200–450  $\text{cm}^{-1}$  in VDOS for HDA (Fig. 17). The overall profile is consistent with previous experimental findings [263, 264].

HDA Si obtained in Morishita's simulation shares traits with the  $\beta$ -tin form in the short-range atomic configuration. Both forms contain distorted tetrahedral configurations with  $N_c$  of 5–6. However, ab initio calculations by Durandurdu and Drabold [266] demonstrated that other types of high-density amorphous Si could be formed by densification. On the basis of DFT calculation with a local-orbital basis set, they simulated a dynamical relaxation process from 800 K to 0 K for the LDA form at various pressures in the range of 0–17 GPa. The LDA form was preserved up to  $\sim 16$  GPa, but it relaxed to a completely different amorphous form at a slightly higher pressure (16.25 GPa). The density of the resultant amorphous form is over 20% higher than that of the LDA form, and it is still higher than that of the HDA form obtained in Morishita's calculation [265]. We thus call this amorphous form VHDA Si to echo the terminology used to describe VHDA ice [152, 171, 265]. The characteristics of  $g(r)$  for the VHDA form (Fig. 18) are similar to those of the HDA form. However, the  $N_c$  of VHDA is 8–9, which is much higher than that of HDA. The atomic configurations in VHDA, in fact, seem to contain fragments of the simple-hexagonal (sh) structure whose  $N_c$  is 8. Note that the sh structure is experimentally obtained by pressurizing the  $\beta$ -tin structure of Si above  $\sim 16$  GPa. [255]. VHDA Si is also found to be metallic and to have a relatively structureless profile of VDOS (Fig. 18).

These theoretical studies suggest the possibility of multiple amorphous–amorphous transitions in Si like those observed in water, although this has not yet been confirmed experimentally (Fig. 19). The notable point is that the pressure-induced sequence of amorphous Si (LDA, HDA, and VHDA) resembles that of crystalline Si (the diamond,  $\beta$ -tin, and sh structures [255]). This similarity suggests that amorphous structures are formed based on the corresponding crystalline structures according to the external pressure. We would like to point out, however, that many metastable crystalline structures are observed in Si [255]. This means that the free energy landscape is immensely complicated, and many local minima, each corresponding to an amorphous or crystalline form, are located in the landscape. It is therefore likely that many variants of the HDA or VHDA forms can be observed experimentally, depending on the sample preparation as well as on the external conditions (temperature and pressure).

Very recently, the structure of HDA-Si was experimentally disclosed by means of X-ray diffraction measurements [267, 268]. Daisenberger et al. [267] have attempted to obtain the structure factor  $S(Q)$  for the HDA form under pressure. Figure 20 shows the experimentally obtained  $S(Q)$  for LDA (3–13.5 GPa) and HDA (16.5 GPa). As the pressure is increased from 13.5 to 16.5 GPa, the first peak becomes more intense than the second peak and shifts to larger  $Q$ . The shift of the first peak indicates a large densification, and the overall features are in good agreement with the ab initio MD results [265] (Fig.16). Unfortunately, however,  $g(r)$  calculated from the  $S(Q)$  by Fourier transformation

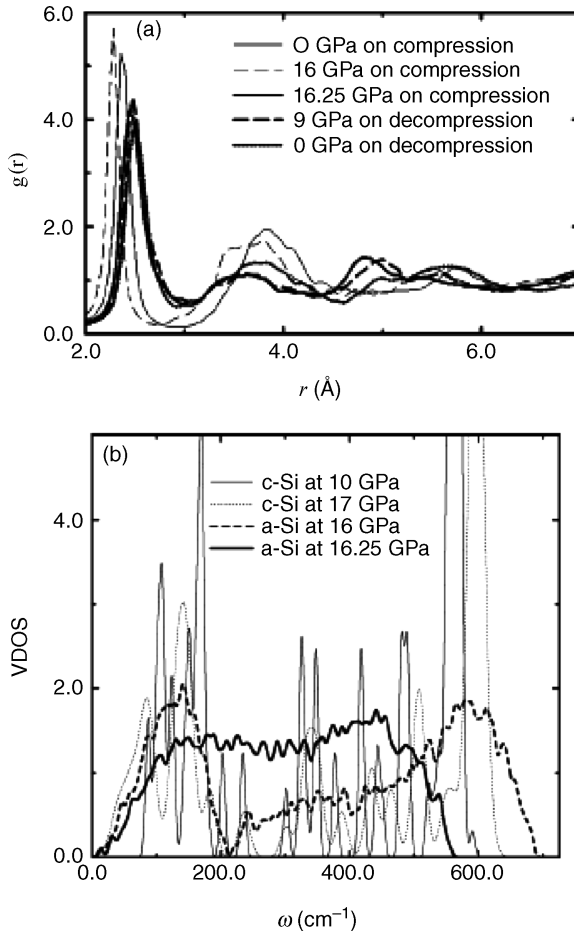


**Figure 18.** (a) Pair correlation functions  $g(r)$  for a-Si at various pressures. (b) VDOS for c- and a-Si at various pressures. Both  $g(r)$  and VDOS were obtained from the DFT calculations with a local-orbital basis set [266].

has insufficient accuracy to compare it with the theoretical  $g(r)$  because of the finite  $Q$  range. Partial recrystallization to the  $\beta$ -tin phase during the measurements also made it difficult to refine the raw  $S(Q)$  data. These problems prevent us from obtaining real-space structural information such as  $g(r)$  and  $N_c$ . To gain deeper insights into the HDA structure, Daisenberger et al. also performed classic MD simulations of the LDA–HDA transition [267, 268] using the Stillinger–Weber (SW) potential [269]. Their MD results are consistent with their experiment and the previous ab initio MD result [265], and concluded that fivefold-coordinated Si atoms are a major component of the HDA structure.

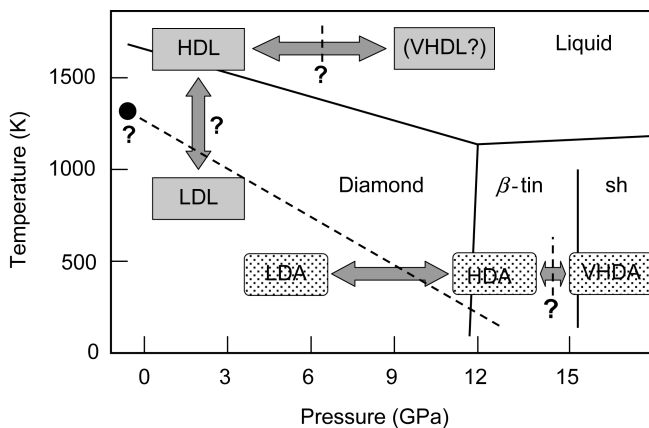


**Figure 19.** Schematic phase relations of Si. Solid lines are the boundaries between liquid and crystalline or crystalline and crystalline phases. Dashed lines denote possible boundaries between amorphous and amorphous or amorphous and liquid (metastable) phases. The filled circle denotes the hypothesized second critical point. Note that the scale of pressure and temperature is uncertain.

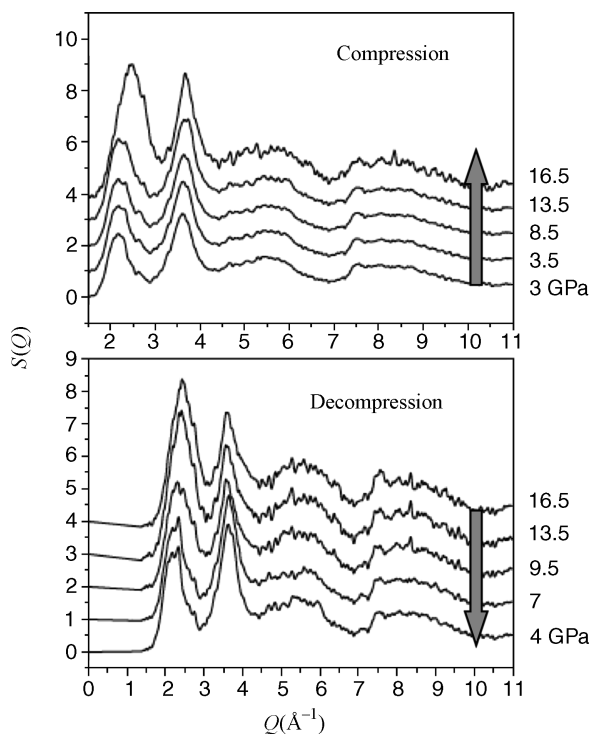


**Figure 20:** Structure factor  $S(Q)$  for a-Si obtained from X-ray diffraction experiments [267]. The sample was first compressed up to  $\sim 17$  GPa and was then decompressed. The LDA–HDA transition took place between 13.5 and 16.5 GPa in the compression process.

Experimental difficulties often lie in obtaining structural data of metastable (amorphous) forms under pressure. Simulation results that complement experimental results are therefore of significant help to interpret experimental data, as demonstrated by Daisenberger et al.

### C. Amorphous Ge

In contrast to what is known about *a*-Si, much less is understood about polyamorphism in Ge. The authors of most early experiments reported no direct evidence of LDA–HDA transition in Ge [260–262, 270, 271]. Shimomura et al. [260] observed a stepwise drop of the electronic resistance (at 6 and 10 GPa) after compression of an *a*-Ge film. This decrease, however, may have resulted from (partial) recrystallization to a metallic high-pressure polymorph under pressure. Tanaka [270] measured X-ray diffraction patterns and optical absorption spectra of *a*-Ge at pressures up to 10 GPa. In this experiment, the sample was indeed partly transformed to the  $\beta$ -tin crystalline phase ( $\sim 25\%$  in volume) at 6 GPa. Imai et al. [262] also observed an amorphous to  $\beta$ -tin crystal transition. Freund et al. [271], in contrast, have observed no sign of crystallization or transition to an HDA form after compression up to  $\sim 9$  GPa.

Although LDA–HDA transitions were not observed directly in these experiments, recent experimental [272] and theoretical studies [273] have demonstrated that Ge actually exhibits amorphous–amorphous transition. Using X-ray absorption spectroscopy (XAS), Principi et al. [272] have detected an abrupt change in the local structure and electronic states at  $\sim 8$  GPa in a compression–decompression cycle of *a*-Ge. The first-neighbor average distance gradually shrank during compression, but it abruptly expanded at  $\sim 8$  GPa. This structural transition is, in contrast to *a*-Si, irreversible: The modified XAS spectra above 8 GPa was preserved after decompression to 0 GPa (Fig. 21). The obtained new amorphous form shows signatures of a metallic character, and its  $N_c$  is roughly estimated to be  $\sim 4.5$  (increase by  $\sim 12\%$ ).

Ab initio calculations by Durandurdu and Drabold [273] also support the existence of amorphous–amorphous transition in Ge. They found that LDA Ge was abruptly transformed to an HDA form at 12.75 GPa by using the same computational protocol as that used in their LDA–VHDA transition study of Si [266]. The density of the resultant HDA form is about 20% higher than that of LDA Ge, and its  $N_c$  is calculated as  $\sim 8$ . This HDA form therefore strongly resembles the VHDA form of Si, rather than the HDA form of Si. This simulation in passing shows that the transition is irreversible, which is consistent with the experiment by Principi et al. [272].

A tight-binding (TB) MD study to examine the pressure effect on structural and dynamical properties of *a*-Ge has also been reported [274]. The calculations were performed based on the order- $N$  nonorthogonal TB framework using the Fermi operator expansion method [275]. The TB MD calculations were run with

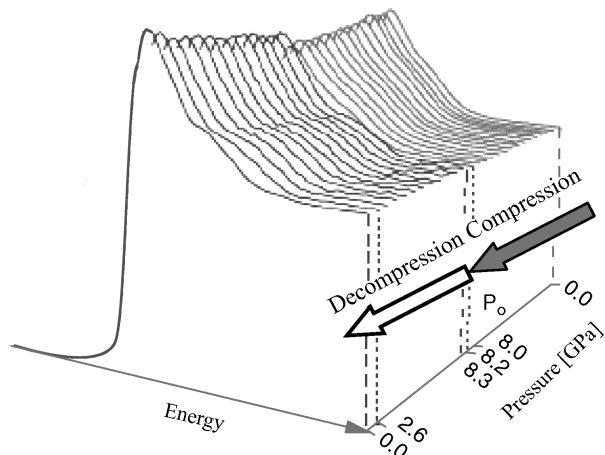


**Figure 21.** X-ray absorption spectroscopy data of *a*-Ge in a compression–decompression cycle [272]. See color insert.

linear 1% increases in density from 4.79 (LDA Ge) to 7.69 g/cm<sup>3</sup>. Only a gradual structural change was observed with increasing density, but the first-peak position of  $g(r)$  showed anomalous density dependence: It shifted to smaller  $r$  as the density was increased up to 6.0 g/cm<sup>3</sup> but then began to shift to larger  $r$  with the density up to 7.0 g/cm<sup>3</sup>. Although no abrupt structural change was observed, an HDA form structurally based on the  $\beta$ -tin structure was found to be formed at the density above  $\sim 6.5$  g/cm<sup>3</sup>. The  $\beta$ -tin structure of Ge is experimentally stable in a very wide pressure range (10–75 GPa) [255]. Thus, the formation of such a “ $\beta$ -tin-like” HDA form is highly plausible. It is worth noting that, in a recent experiment, vitrification of *l*-Ge under pressure has been attempted, where the “ $\beta$ -tin-like” HDA Ge is expected to form [276].

Unfortunately, the experimental and theoretical studies described above do not provide a consistent picture of polyamorphic transformations of Ge. The *ab initio* calculations [273] have predicted a highly densified *a*-Ge with  $N_c$  of  $\sim 8$ , which may be categorized as VHDA (a third amorphous form). However, considering the stability of the  $\beta$ -tin structure in a wide pressure range, a “ $\beta$ -tin-like” HDA form is more likely to be formed in Ge, as suggested in Refs. [272, 274, and 276]. Additional experimental evidence is eminently desirable.

#### D. Liquid Si and Ge (*l*-Si and *l*-Ge)

The discovery of multiple amorphous phases has put the spotlight on underlying liquid–liquid (L–L) transitions. Here, attempts thus far to discover possible L–L transitions of Si and Ge will be briefly reviewed. By analogy with L–L transition

in water, supercooling *l*-Si or Ge is a promising route to induce possible L–L (HDL–LDL) transitions (see Fig. 19).

Many experiments have been conducted to measure  $S(Q)$  and density, as well as other thermodynamic properties, such as heat capacity, of supercooled *l*-Si using the containerless levitation technique [277–286]. Almost the same profile of  $S(Q)$  is obtained in all these experiments around the melting temperature (1687 K). However, different tendencies of structural changes during supercooling have been reported among these experiments. For instance, some experiments show that  $N_c$  decreases during cooling [277, 279], whereas others show that  $N_c$  increases or is retained at a constant down to  $\sim 1400$  K (Fig. 22) [278, 280, 281]. This inconsistency in structural information may partially come from the enormous difficulty in measuring supercooled *l*-Si in situ, which results in the strong dependence on each experimental measurement. Interestingly, based on their experimental finding that  $N_c$  is constant during supercooling, Kim et al. [280] have concluded that Si exhibits no L–L transition.

A recent ab initio MD study [287] has revealed an anomalous structural change of *l*-Si after cooling and has resolved the controversial experimental findings described above. This ab initio (plane wave DFT) study has shown that  $N_c$  is indeed constant after supercooling down to  $\sim 1400$  K, as found experimentally by Kim et al. [280] and Higuchi et al. [281]. However, the calculations have also shown that  $N_c$  begins to decrease below  $\sim 1200$  K, the temperature at which the density maximum occurs [287] (Fig. 22). The tetrahedral network structure is found to grow rapidly during cooling below  $\sim 1200$  K, which has called Kim’s conclusion (no L–L transition) into question (note that no experimental measurement is currently accessible below  $\sim 1350$  K).

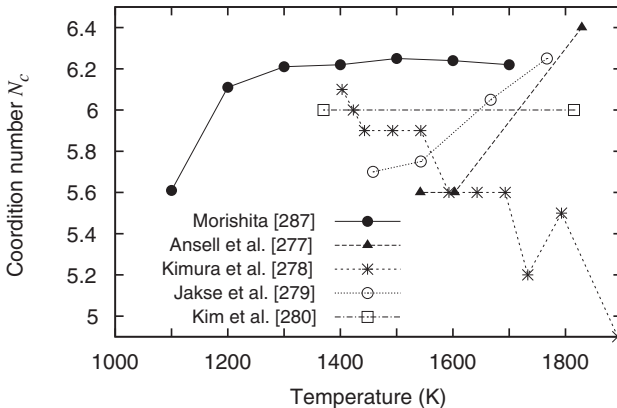


**Figure 22.** Temperature dependence of  $N_c$  in *l*-Si during supercooling. All data are experimentally obtained [277–280], except those indicated by the filled circles, which are the ab initio MD results [287].

Clear evidence of L–L transitions has been found only in *l*-Si modeled by the SW potential [269]. Sastry and Angell [288] performed MD simulations of supercooled *l*-Si using the SW potential. After cooling at ambient pressure, the liquid (HDL) was transformed to LDL at  $\sim 1060$  K. The  $N_c$  in LDL is almost 4, and the diffusivity is low compared with that in HDL. The structural properties of LDL, such as  $g(r)$  and  $N_c$ , are very close to those of LDA, which indicates that this HDL–LDL transition is a manifestation of the multiple amorphous forms (LDA and HDA) of Si. McMillan et al. [264] and Morishita [289] have also found structural fluctuations between LDL-like and HDL-like forms in their MD calculations for *l*-Si at 1100 K. Morishita has demonstrated that such a structural fluctuation induces spatial and temporal dynamical heterogeneity, and this heterogeneity accounts for the non-Debye relaxation process that becomes noticeable in the supercooled state [289].

However, we point out that the nature of the L–L transition in SW MD calculations strongly depends on the external conditions and details of the parameters used in the SW potential [290]. For instance, a slight change of the external pressure simply results in a gradual structural change during supercooling [290]. In fact, the SW model gives much lower density than the experimental density for *l*-Si at ambient pressure [289]. An external pressure of 5–6 GPa is necessary to obtain the experimental density in the SW model, but the L–L transition can never be observed under this pressure, and the liquid simply vitrifies to an HDA-like solid [287, 289, 291]. Additional improvements in both experiments and theoretical calculations are thus necessary to clarify whether *l*-Si actually exhibits L–L transitions.

The situation is the same in *l*-Ge. Although X-ray absorption measurements [292] and TB MD calculations [293] have been carried out for supercooled *l*-Ge, L–L transitions have not yet been firmly confirmed.

Pressurization is another possible way to observe L–L transitions or related phenomena (Fig. 19), but many difficulties lie in measuring *l*-Si and *l*-Ge in situ under high pressure. Therefore, only a few experimental studies have been reported to date [294–296]. Tsuji and colleagues measured *l*-Si and *l*-Ge in relatively wide pressure ranges: 4–23 GPa for *l*-Si [294] and 1–25 GPa for *l*-Ge [295, 296]. Although no discontinuous structural change was observed in either liquid, anomalous pressure dependence of the nearest neighbor distance was revealed in *l*-Si, which expanded about 1.6% between 8 and 14 GPa despite the pressurization. This finding may reflect an underlying drastic structural change at lower temperatures (likely below the melting lines; see Fig. 19). It was also found that anisotropy of the local structure in *l*-Ge, which is estimated by the ratio of the second peak position to the first peak position of  $S(Q)$ , persists up to 25 GPa.

Simulation studies [297, 298] have supported the experimental results of Tsuji et al. [295]. In addition to structural information, ab initio MD

calculations have predicted dynamical properties of *l*-Si under pressure, such as the intermediate scattering function  $F(q, t)$  [297] and self-diffusion coefficients  $D$  [298]. What should be stressed here is that deeply supercooled *l*-Si exhibits anomalous pressure dependence of the diffusivity [298]. At 1100 K,  $D$  increases as the pressure increases up to  $\sim 10$  GPa, but it begins to decrease above  $\sim 10$  GPa. This diffusive anomaly has already been observed in water [299, 300] and silicate melts [301–303], and it is attributed to the collapse of the open tetrahedral network by densification. The fact that the diffusive anomaly is also exhibited in *l*-Si strongly suggests that tetrahedrally coordinated liquids (e.g., water, silicate melts, and *l*-Si) share common characteristics that would play a fundamental role in polyamorphism in these substances.

## V. DISCUSSION AND CONCLUSIONS

Overall, recent experimental and theoretical studies have supported the existence of multiple amorphous phases in oxide glasses, water, and semiconductors. Although many parallels exist regarding the amorphous–amorphous transitions, there are also substantial differences. Parallels include the change of coordination number and intermediate range order during compression while retaining an amorphous character. The most prominent difference is the sharp transition with a possible first-order nature from LDA-water to HDA-water, which has not been observed in any other substance. Of course, also temperature and pressure ranges where the transitions are observed differ substantially because of the different interactions involved (e.g., hydrogen-bond interaction versus van der Waals interaction). However, the continuous HDA–VHDA transition in water resembles the broader transitions also observed in silica, even though the nature of intermolecular forces is different.

In the case of oxides, one can conclude that transformations in the glasses in many respects are similar to the transitions that occur in their crystalline counterparts. The most prominent phenomenon in the oxide glasses under compression is coordination increase: 4-to-6 in the case of a-SiO<sub>2</sub> and a-GeO<sub>2</sub>, and 3-to-4 in the case of a-B<sub>2</sub>O<sub>3</sub>. Computer simulations predict an additional increase of coordination number at pressures exceeding 100 GPa—up to 8 for a-SiO<sub>2</sub> and a-GeO<sub>2</sub>, and up to 6 for a-B<sub>2</sub>O<sub>3</sub>, with the analogy of corresponding crystalline substances. These transformations still have to be discovered experimentally in the future. However, several aspects of the phase transition delineate the behavior of oxide glasses from the behavior in the crystals. The coordination transformation occurs in broad pressure intervals and intermediate coordination—five-fold, which does not exist in the crystalline high-pressure modifications, is very important in the case of a-SiO<sub>2</sub> and a-GeO<sub>2</sub>. Second, in all glasses at lower pressures there are transformations, which modify the intermediate-range order (ring-statistics etc.). These transformations are

strongly promoted by heating under pressure, and they have no direct analogs in the corresponding crystals.

In the case of water, the three amorphous states LDA, HDA, and VHDA can be distinguished by the number zero, one, or two interstitial water molecules near the faces of the tetrahedron called the “Walrafen pentamer.” The tetrahedron itself is not much distorted except for a slight increase of OO-distance caused by the repulsion of interstitial water molecules. Recent studies have suggested that a clear distinction between structurally unrelaxed HDA (uHDA) and structurally relaxed HDA (eHDA or VHDA) has to be made in the future. Although currently it is not entirely clear whether the amorphous ices are glasses structurally related to deeply supercooled liquids or nanocrystals, this distinction may help in sorting out the issue. It is clear now that there is at most one first-order-like transition in amorphous ices and in addition a continuous transition taking place in a finite pressure interval.

In case of Si, it seems that the degree of tetrahedrality is the key to characterizing disordered phases. Degradation of tetrahedrality in HDA Si is moderate, whereas that in VHDA Si is considerable. The striking similarity between the pressure-induced transition sequence of *a*-Si (LDA-HDA-VHDA) and that of *c*-Si (D- $\beta$ -tin-sh) may give a hint to the essential mechanism for polyamorphism in Si. We would like to stress that many metastable crystalline phases such as BC8 (Si-III) have been observed in Si [252], which indicates that the free energy landscape is likely to be highly complicated and that many variations of each amorphous form may be formed.

Although supporting evidence of the multiple amorphous phases in Ge is not currently sufficient, it seems likely that Ge exhibits amorphous–amorphous and L–L transitions by analogy with Si. It is worth noting that the  $\beta$ -tin phase in Ge is stable in an extremely wide pressure range (10–75 GPa) compared with the  $\beta$ -tin Si phase (10–16 GPa) [252]. The third amorphous phase in Ge (e.g., VHDA Ge) could therefore be expected to form at relatively high pressures (if such a phase exists). It is known that the large *3d*-electron core radius, which is absent in Si, accounts for the high stability of  $\beta$ -tin Ge over a wide pressure range. Such an effect of the electronic properties on structural stability is of course significant in amorphous solids. Because the interatomic interaction (electronic structure) plays a fundamental role in polyamorphism, a microscopic description that includes the electronic structure is indispensable for profound understanding of polyamorphism, particularly in semiconductors such as Si and Ge.

### Acknowledgments

T.L. is grateful to his M.Sc. and Ph.D. students, Katrin Winkel, Marion Bauer, Michael Elsaesser, Markus Seidl, and Juergen Bernard, for their devotion to the subject and for discussion, to Erwin Mayer for inspiring many experiments and improving the manuscript, to the Austrian Science Fund (FWF projects R37-N11 and Y391), and to the European Research Council (ERC Starting Grant,

SULIWA) for financial support. V.B. is grateful to A.G. Lyapin, O.B. Tsiok, K. Trachenko, and Y. Katayama for their help and useful discussions and to the Russian Foundation for Basic Research (07-02-01275 and 08-02-00014) and the Programs of the Presidium of RAS for financial support. T.M. is grateful to O. Mishima and T. Ikeshoji for useful discussion and to the Ministry of Education, Culture, Sports, Science and Technology, Japan for financial support.

## References

1. R. Zallen, *The Physics of Amorphous Solids*, Wiley, New York, 1983.
2. S. R. Elliott, *Physics of Amorphous Materials*, Longman Group Limited, New York, 1983.
3. J. Zarzycki, *Glasses and the Vitreous State*, Cambridge University Press, Cambridge, UK, 1991.
4. P. M. Ossi, *Disordered Materials—An Introduction*, 2nd ed., Springer-Verlag, Berlin, Germany, 2006.
5. G. P. Johari, *J. Chem. Edu.* **51**, 23 (1974).
6. W. Kauzmann, *Chem. Rev.* **43**, 219 (1948).
7. A. Eisenberg, in *Physical Properties of Polymers* A. E. James E. Mark, William W. Graessley, Leo Mandelkern, Edward T. Samulski, Jack L. Koenig, and George D. Wignall, eds., American Chemical Society, Washington, DC, 1993.
8. C. A. Angell, K. L. Ngai, G. B. McKenna, P. F. McMillan, and S. W. Martin, *Appl. Phys. Rev.* **88**, 3113 (2000).
9. A. Navrotsky, *Nat. Mater.* **2**, 571 (2003).
10. P. F. McMillan, J. Gryko, C. Bull, R. Arledge, A. J. Kenyon, and B. A. Cressey, *J. Solid State Chem.* **178**, 937 (2005).
11. A. Hedoux, Y. Guinet, and M. Descamps, *Phys. Rev. B: Condens. Matt. Mater. Phys.* **58**, 31 (1998).
12. G. P. Johari, S. Ram, G. Astl, and E. Mayer, *J. Non-Cryst. Solids* **116**, 282 (1990).
13. V. A. Likhachev, *Glass Physics and Chemistry (Translation of Fizika i Khimiya Stekla)* **22**, 80 (1996).
14. S. Susman, K. J. Volin, D. L. Price, M. Grimsditch, J. P. Rino, R. K. Kalia, P. Vashishta, G. Gwanmesia, Y. Wang, and R. C. Liebermann, *Phys. Rev. B* **43**, 1194 (1991).
15. T. Grande, S. Stolen, A. Grzechnik, W. A. Crichton, and M. Mezouar, *Physica A* **314**, 560 (2002).
16. S. Sampath, C. J. Benmore, K. M. Lantzky, J. Neufeind, K. Leinenweber, D. L. Price, and J. L. Yarger, *Phys. Rev. Lett.* **90**, 115502/1 (2003).
17. Y. Inamura, Y. Katayama, W. Utsumi, and K.-i. Funakoshi, *Phys. Rev. Lett.* **93**, 015501 (2004).
18. J. Urquidi, C. J. Benmore, P. A. Egelstaff, M. Guthrie, S. E. McLain, C. A. Tulk, D. D. Klug, and J. F. C. Turner, *Molec. Phys.* **102**, 2007 (2004).
19. C. J. Benmore, R. T. Hart, Q. Mei, D. L. Price, J. Yarger, C. A. Tulk, and D. D. Klug, *Phys. Rev. B* **72**, 132201 (2005).
20. D. T. Bowron, J. L. Finney, A. Hallbrucker, I. Kohl, T. Loerting, E. Mayer, and A. K. Soper, *J. Chem. Phys.* **125**, (2006).
21. V. V. Brazhkin, *J. Phys. Condens. Matt.* **18**, 9643 (2006).
22. V. V. Brazhkin, *Phys. Rev. Lett.* **98**, 069601 (2007).
23. J. Bernstein, *Polymorphism in Molecular Crystals*, Oxford University Press, Oxford, UK, 2002.
24. V. V. Brazhkin and A. G. Lyapin, *Jetp. Lett-Engl. Tr.* **78**, 542 (2003).
25. O. Mishima, L. D. Calvert, and E. Whalley, *Nature* **314**, 76 (1985).

26. K. Trachenko, V. V. Brazhkin, O. B. Tsiok, M. T. Dove, and E. K. H. Salje, *Phys. Rev. Lett.* **98**, 135502 (2007).
27. H. W. Sheng, H. Z. Liu, Y. Q. Cheng, J. Wen, P. L. Lee, W. K. Luo, S. D. Shastri, and E. Ma, *Nat. Mater.* **6**, 192 (2007).
28. M. C. Wilding, P. F. McMillan, and A. Navrotsky, *Physica A* **314**, 379 (2002).
29. V. V. Brazhkin, Y. Katayama, M. V. Kondrin, T. Hattori, A. G. Lyapin, and H. Saitoh, *Phys. Rev. Lett.* **100**, 145701/1 (2008).
30. S. V. Buldyrev and H. E. Stanley, *Physica A* **330**, 124 (2003).
31. I. Brovchenko, A. Geiger, and A. Oleinikova, *J. Chem. Phys.* **118**, 9473 (2003).
32. I. Brovchenko, A. Geiger, and A. Oleinikova, *J. Chem. Phys.* **123**, 044515 (2005).
33. I. Brovchenko and A. Oleinikova, *J. Chem. Phys.* **124**, 164505 (2006).
34. P. Jedlovsky and R. Vallauri, *J. Chem. Phys.* **122**, 081101/1 (2005).
35. P. Jedlovsky, L. B. Partay, A. P. Bartok, G. Garberoglio, and R. Vallauri, *J. Chem. Phys.* **126**, 241103/1 (2007).
36. P. Jedlovsky, L. B. Partay, A. P. Bartok, V. P. Voloshin, N. N. Medvedev, G. Garberoglio, and R. Vallauri, *J. Chem. Phys.* **128**, 244503/1 (2008).
37. S. M. Sharma and S. K. Sikka, *Prog. Mater. Sci.* **40**, 1 (1996).
38. H. E. Stanley, *Pramana* **53**, 53 (1999).
39. V. V. Brazhkin, A. G. Lyapin, S. V. Popova, and R. N. Voloshin, *NATO Sci. Ser., II Math., Phys. Chem.* **81**, 15 (2002).
40. P. G. Debenedetti, *J. Phys. Condens. Matter* **15**, R1669 (2003).
41. V. V. Brazhkin, and A. G. Lyapin, *J. Phys. Cond. Matter* **15**, 6059 (2003).
42. P. F. McMillan, *J. Mater. Chem.* **14**, 1506 (2004).
43. J. L. Yarger and G. H. Wolf, *Science* **306**, 820 (2004).
44. C. A. Angell, *Annu. Rev. Phys. Chem.* **55**, 559 (2004).
45. S. Petit and G. Coquerel, *Polymorphism* **259** (2006).
46. T. Loerting, K. Winkel, C. G. Salzmann, and E. Mayer, *Phys. Chem. Chem. Phys.* **8**, 2810 (2006).
47. T. Loerting and N. Giovambattista, *J. Phys. Cond. Matt.* **18**, R919 (2006).
48. G. P. Johari and O. Andersson, *Thermochim. Acta* **461**, 14 (2007).
49. W. B. Hubbard, *Planetary Interiors*, Van Nostrand Reinhold, New York, 1984.
50. D. L. Anderson, *Theory of the Earth.*, Blackwell Scientific Publications, Boston, MA, 1989.
51. R. J. Hemley, J. Badro, and D. M. Teter, *Phys. Meets Min.* 173 (2000).
52. A. Putnis, *Introduction to Mineral Sciences*, Cambridge University Press, Cambridge, U.K., 1992.
53. R. J. Hemley, C. T. Prewitt, and K. J. Kingma, *Rev. Mineral.* **29**, 41 (1994).
54. V. Swamy, S. K. Saxena, B. Sundman, and J. Zhang, *J. Geophys. Res.* **99**, 11 (1994).
55. G. A. Lyzenga, T. J. Ahrens, and A. C. Mitchell, *J. Geophys. Res.* **88**, 2431 (1983).
56. D. R. Schmitt and T. J. Ahrens, *J. Geophys. Res.* **94**, 5851 (1989).
57. J. A. Akins and T. J. Ahrens, *Geophys. Res. Lett.* **29**, 31/1 (2002).
58. D. Andraut, G. Fiquet, F. Guyot, and M. Hanfland, *Science* **282**, 720 (1998).
59. S. Ono, *Abstracts of AGU 2001 Fall Meeting, San Francisco*, 2001.

60. L. S. Dubrovinsky, S. K. Saxena, P. Lazor, R. Ahuja, O. Eriksson, J. M. Wills, and B. Johansson, *Nature* **388**, 362 (1997).
61. Y. Kuwayama, K. Hirose, N. Sata, and Y. Ohishi, *Science* **309**, 923 (2005).
62. S. R. Shieh, T. S. Duffy, and G. Shen, *Earth Planet. Sci. Lett.* **235**, 273 (2005).
63. V. P. Prakapenka, G. Shen, L. S. Dubrovinsky, M. L. Rivers, and S. R. Sutton, *J. Phys. Chem. Solids* **65**, 1537 (2004).
64. A. G. Lyapin, V. V. Brazhkin, E. L. Gromnitskaya, O. V. Stal'gorova, and O. B. Tsiok, *Phys. Uspokhi* **42**, 1059 (1999).
65. A. G. Lyapin, V. V. Brazhkin, E. L. Gromnitskaya, V. V. Mukhamadiarov, O. V. Stal'gorova, and O. B. Tsiok, *NATO Sci. Ser., II Math., Phys. Chem.* **81**, 449 (2002).
66. P. W. Bridgman and I. Simon, *J. Appl. Phys.* **24**, 405 (1953).
67. H. M. Cohen and R. Roy, *Phys. Chem. Glasses* **6**, 149 (1965).
68. M. Grimsditch, *Phys. Rev. Lett.* **52**, 2379 (1984).
69. R. J. Hemley, H. K. Mao, P. M. Bell, and B. O. Mysen, *Phys. Rev. Lett.* **57**, 747 (1986).
70. M. Grimsditch, *Phys. Rev. B* **34**, 4372 (1986).
71. T. Gerber, B. Himmel, H. Lorenz, and D. Stachel, *Cryst. Res. Technol.* **23**, 1293 (1988).
72. C. Meade, R. J. Hemley, and H. K. Mao, *Phys. Rev. Lett.* **69**, 1387 (1992).
73. C.-s. Zha, R. J. Hemley, H.-k. Mao, T. D. Duffy, and C. Meade, *Phys. Rev. B: Condens. Matt.* **50**, 13105 (1994).
74. E. M. Stolper and T. J. Ahrens, *Geophys. Res. Lett.* **14**, 1231 (1987).
75. V. G. Karpov and M. Grimsditch, *Phys. Rev. B Condens. Matt.* **48**, 6941 (1993).
76. O. B. Tsiok, V. V. Brazhkin, A. G. Lyapin, and L. G. Khvostantsev, *Phys. Rev. Lett.* **80**, 999 (1998).
77. L. Stixrude and M. S. T. Bukowinski, *Phys. Rev. B Condens. Matt.* **44**, 2523 (1991).
78. J. S. Tse, D. D. Klug, and Y. Le Page, *Phys. Rev. B Condens. Matt.* **46**, 5933 (1992).
79. R. G. Della Valle and E. Venuti, *Phys. Rev. B Condens. Matt.* **54**, 3809 (1996).
80. D. J. Lacks, *Phys. Rev. Lett.* **80**, 5385 (1998).
81. D. J. Lacks, *Phys. Rev. Lett.* **84**, 4629 (2000).
82. E. Demiralp, T. Cagin, and W. A. Goddard, III, *Phys. Rev. Lett.* **82**, 1708 (1999).
83. J. R. Rustad, D. A. Yuen, and F. J. Spera, *Phys. Rev. B Condens. Matt.* **44**, 2108 (1991).
84. Y. Inamura, M. Arai, N. Kitamura, S. M. Bennington, and A. C. Hannon, *Physica B* **241-243**, 903 (1998).
85. G. D. Mukherjee, S. N. Vaidya, and V. Sugandhi, *Phys. Rev. Lett.* **87**, 195501 (2001).
86. P. McMillan, B. Piriou, and R. Couty, *J. Chem. Phys.* **81**, 4234 (1984).
87. T. Rouxel, H. Ji, T. Hammouda, and A. Moreac, *Phys. Rev. Lett.* **100**, 225501/1 (2008).
88. R. A. B. Devine, R. Dupree, I. Farnan, and J. J. Capponi, *Phys. Rev. B Condens. Matt.* **35**, 2560 (1987).
89. V. P. Prakapenka, G. Shen, M. L. Rivers, and S. R. Sutton, *AGU Fall Meet. Suppl. Abstract* **84**, V41E (2003).
90. F. S. El'kin, V. V. Brazhkin, L. G. Khvostantsev, O. B. Tsiok, and A. G. Lyapin, *JETP Lett.* **75**, 342 (2002).
91. K. Trachenko, M. T. Dove, V. Brazhkin, and F. S. El'kin, *Phys. Rev. Lett.* **93**, 135502 (2004).
92. K. Trachenko and M. T. Dove, *Phys. Rev. B Condens. Matt. Mater. Phys.* **67**, 064107/1 (2003).

93. M. F. Thorpe, *J. Non-Cryst. Solids* **57**, 355 (1983).
94. J.-F. Lin, H. Fukui, D. Prendergast, T. Okuchi, Y. Q. Cai, N. Hiraoka, C.-S. Yoo, A. Trave, P. Eng, M. Y. Hu, and P. Chow, *Phys. Rev. B Condens. Matter* **75**, 012201/1 (2007).
95. H. Fukui, M. Kanzaki, N. Hiraoka, and Y. Q. Cai, *Phys. Rev. B Condens. Matter* **78**, 012203/1 (2008).
96. S. K. Lee, P. J. Eng, H.-k. Mao, Y. Meng, and J. Shu, *Phys. Rev. Lett.* **98**, 105502/1 (2007).
97. S. K. Lee, P. J. Eng, H.-k. Mao, Y. Meng, M. Newville, M. Y. Hu, and J. Shu, *Nature Mat.* **4**, 851 (2005).
98. V. V. Brazhkin and K. Trachenko, unpublished data.
99. M. Kanzaki, *J. Am. Ceram. Soc.* **73**, 3706 (1990).
100. E. Ohtani, F. Taulelle, and C. A. Angell, *Nature* **314**, 78 (1985).
101. X. Xue, J. F. Stebbins, M. Kanzaki, and R. G. Tronnes, *Science* **245**, 962 (1989).
102. J. Zhang, R. C. Liebermann, T. Gasparik, C. T. Herzberg, and Y. Fei, *J. Geophys. Res.* **98**, 19785 (1993).
103. I. Saika-Voivod, F. Sciortino, and P. H. Poole, *Phys. Rev. E* **63**, 11202 (2000).
104. J. Horbach, *J. Phys. Condens. Matter* **20**, 244118/1 (2008).
105. P. K. Hung, N. V. Hong, and L. T. Vinh, *J. Phys. Condens. Matter* **19**, 466103/1 (2007).
106. V. B. Prakapenka, L. S. Dubrovinsky, G. Shen, M. L. Rivers, S. R. Sutton, V. Dmitriev, H. P. Weber, and T. Le Bihan, *Phys. Rev. B Condens. Matter* **67**, 132101/1 (2003).
107. S. Ono, T. Tsuchiya, K. Hirose, and Y. Ohishi, *Phys. Rev. B Condens. Matter* **68**, 014103/1 (2003).
108. C. E. Stone, A. C. Hannon, T. Ishihara, N. Kitamura, Y. Shirakawa, R. N. Sinclair, N. Umesaki, and A. C. Wright, *J. Non-Cryst. Solids* **293-295**, 769 (2001).
109. J. P. Itie, A. Polian, G. Calas, J. Petiau, A. Fontaine, and H. Tolentino, *Phys. Rev. Lett.* **63**, 398 (1989).
110. K. H. Smith, E. Shero, A. Chizmeshya, and G. H. Wolf, *J. Chem. Phys.* **102**, 6851 (1995).
111. M. Guthrie, C. A. Tulk, C. J. Benmore, J. Xu, J. L. Yarger, D. D. Klug, J. S. Tse, H. K. Mao, and R. J. Hemley, *Phys. Rev. Lett.* **93**, 115502/1 (2004).
112. X. Hong, G. Shen, V. B. Prakapenka, M. Newville, M. L. Rivers, and S. R. Sutton, *Phys. Rev. B Condens. Matter* **75**, 104201/1 (2007).
113. M. Micoulaut, L. Cormier, and G. S. Henderson, *J. Phys. Condens. Matter* **18**, R753 (2006).
114. K. V. Shanavas, N. Garg, and S. M. Sharma, *Phys. Rev. B Condens. Matter* **73**, 094120/1 (2006).
115. G. Shen, H.-P. Liermann, S. Sinogeikin, W. Yang, X. Hong, C.-S. Yoo, and H. Cynn, *Proc. Natl. Acad. Sci. U.S.A.* **104**, 14576 (2007).
116. A. G. Lyapin, V. V. Brazhkin, Y. Katayama, and Y. Inamura, *Abstracts of Joint 21st AIRAPT and 45th EHPRG International Conference, Catania, 2007*, 246.
117. O. Ohtaka, H. Arima, H. Fukui, W. Utsumi, Y. Katayama, and A. Yoshiasa, *Phys. Rev. Lett.* **92**, 155506/1 (2004).
118. V. V. Hoang, N. H. T. Anh, and H. Zung, *Phys. B* **390**, 17 (2007).
119. J. Krogh-Moe, *J. Non-Cryst. Solids* **1**, 269 (1969).
120. D. R. Uhlmann, J. F. Hays, and D. Turnbull, *Phys. Chem. Glasses* **8**, 1 (1967).
121. J. D. Mackenzie, *J. Am. Ceram. Soc.* **46**, 461 (1963).
122. A. C. Wright, C. E. Stone, R. N. Sinclair, N. Umesaki, N. Kitamura, K. Ura, N. Ohtori, and A. C. Hannon, *Phys. Chem. Glasses* **41**, 296 (2000).
123. E. Chason and F. Spaepen, *J. Appl. Phys.* **64**, 4435 (1988).

124. M. Grimsditch, R. Bhadra, and Y. Meng, *Phys. Rev. B Condens. Matter Phys.* **38**, 7836 (1988).
125. J. Nicholas, S. Sinogeikin, J. Kieffer, and J. Bass, *Phys. Rev. Lett.* **92**, 215701/1 (2004).
126. M. Grimsditch, A. Polian, and A. C. Wright, *Phys. Rev. B Condens. Matter.* **54**, 152 (1996).
127. A. Takada, *Phys. Chem. Glasses* **45**, 156 (2004).
128. L. Huang, J. Nicholas, J. Kieffer, and J. Bass, *J. Phys. Condens. Matter* **20**, 075107/1 (2008).
129. V. V. Brazhkin, Y. Katayama, K. Trachenko, O. B. Tsiok, A. G. Lyapin, E. Artacho, M. Dove, G. Ferlat, Y. Inamura, and H. Saitoh, *Phys. Rev. Lett.* **101**, 035702 (2008).
130. T. Hattori, T. Kinoshita, T. Narushima, K. Tsuji, and Y. Katayama, *Phys. Rev. B Condens. Matter Phys.* **73**, 054203/1 (2006).
131. G. Widmann and R. Riesen, *J. Thermal Anal. Calorim.* **52**, 109 (1998).
132. E. F. Burton and W. F. Oliver, *Proc. R. Soc. Ser. A* **153**, 166 (1935).
133. E. F. Burton and W. F. Oliver, *Nature* **135**, 505 (1935).
134. E. Mayer and R. Pletzer, *Nature* **319**, 298 (1986).
135. R. Pletzer and E. Mayer, *J. Chem. Phys.* **90**, 5207 (1989).
136. E. Mayer and R. Pletzer, *J. Phys. Colloq.* **48**, 581 (1987).
137. Z. Dohnalek, G. A. Kimmel, P. Ayotte, R. S. Smith, and B. D. Kay, *J. Chem. Phys.* **118**, 364 (2003).
138. A. Hallbrucker, E. Mayer, and G. P. Johari, *J. Phys. Chem.* **93**, 4986 (1989).
139. P. Jenniskens and D. F. Blake, *Science* **265**, 753 (1994).
140. P. Jenniskens, D. F. Blake, M. A. Wilson, and A. Pohorille, *Astrophys. J.* **455**, 389 (1995).
141. P. Jenniskens and D. F. Blake, *Planet. Space Sci.* **44**, 711 (1996).
142. B. Guillot and Y. Guissani, *J. Chem. Phys.* **120**, 4366 (2004).
143. P. Parent, S. Lacombe, F. Bournel, and C. Laffon, *Physics and Chemistry of Ice*, W. F. Kuhs, ed., RSC Publishing, Cambridge, U.K., 2007.
144. P. Braggeller and E. Mayer, *Nature* **288**, 569 (1980).
145. E. Mayer and P. Brueggeller, *Nature* **298**, 715 (1982).
146. E. Mayer, *J. Appl. Phys.*, **58**, 663 (1985).
147. V. F. Petrenko and R. W. Whitworth, *Physics of Ice*, Oxford University Press, Oxford, U.K., 1999.
148. M. Bauer, M. S. Elsaesser, K. Winkel, E. Mayer, and T. Loerting, *Phys. Rev. B* **77**, 220105/1 (2008).
149. O. Mishima, L. D. Calvert, and E. Whalley, *Nature* **310**, 393 (1984).
150. T. Loerting, I. Kohl, W. Schustereder, A. Hallbrucker, and E. Mayer, *Chem. Phys. Chem.* **7**, 1203 (2006).
151. J. S. Tse, D. D. Klug, C. A. Tulk, I. Swainson, E. C. Svensson, C. K. Loong, V. Shpakov, V. R. Belosludov, R. V. Belosludov, and Y. Kawazoe, *Nature* **400**, 647 (1999).
152. T. Loerting, C. Salzmann, I. Kohl, E. Mayer, and A. Hallbrucker, *Phys. Chem. Chem. Phys.* **3**, 5355 (2001).
153. O. Mishima, *J. Chem. Phys.* **100**, 5910 (1994).
154. K. Winkel, M. S. Elsaesser, M. Seidl, M. Bauer, E. Mayer, and T. Loerting, *J. Phys. Cond. Matt.* in press.
155. K. Winkel, M. S. Elsaesser, E. Mayer, and T. Loerting, *J. Chem. Phys.* **128**, 044510/1 (2008).
156. C. G. Salzmann, E. Mayer, and A. Hallbrucker, *Phys. Chem. Chem. Phys.* **6**, 1269 (2004).

157. J. E. Bertie, L. D. Calvert, and E. Whalley, *J. Chem. Phys.* **38**, 840 (1963).
158. J. E. Bertie, L. D. Calvert, and E. Whalley, *Can. J. Chem.* **42**, 1373 (1964).
159. D. D. Klug, Y. P. Handa, J. S. Tse, and E. Whalley, *J. Chem. Phys.* **90**, 2390 (1989).
160. A. I. Kolesnikov, V. V. Sinitsyn, E. G. Ponyatovsky, I. Natkaniec, L. S. Smirnov, and J. C. Li, *J. Phys. Chem. B* **101**, 6082 (1997).
161. Y. Yoshimura, S. T. Stewart, M. Somayazulu, H.-k. Mao, and R. J. Hemley, *J. Chem. Phys.* **124**, 024502 (2006).
162. C. McBride, C. Vega, E. Sanz, and J. L. F. Abascal, *J. Chem. Phys.* **121**, 11907 (2004).
163. Y. Yoshimura, H.-k. Mao, and R. J. Hemley, *Chem. Phys. Lett.* **420**, 503 (2006).
164. N. Sartori, J. Bednar, and J. Dubochet, *J. Microscop.* **182**, 163 (1996).
165. G. A. Baratta, G. Leto, F. Spinella, G. Strazzulla, and G. Foti, *Astron. Astrophys.* **252**, 421 (1991).
166. A. Kouchi and T. Kuroda, *Nature* **344**, 134 (1990).
167. G. Leto and G. A. Baratta, *Astron. Astrophys.* **397**, 7 (2003).
168. M. H. Moore and R. L. Hudson, *Astrophys. J.* **401**, 353 (1992).
169. R. L. Hudson and M. H. Moore, *J. Phys. Chem.* **96**, 6500 (1992).
170. O. Mishima, *Nature* **384**, 546 (1996).
171. J. L. Finney, D. T. Bowron, A. K. Soper, T. Loerting, E. Mayer, and A. Hallbrucker, *Phys. Rev. Lett.* **89**, 205503 (2002).
172. C. G. Salzmann, T. Loerting, S. Klotz, P. W. Mirwald, A. Hallbrucker, and E. Mayer, *Phys. Chem. Chem. Phys.* **8**, 386 (2006).
173. T. Loerting, W. Schustereder, K. Winkel, C. G. Salzmann, I. Kohl, and E. Mayer, *Phys. Rev. Lett.* **96**, 025702 (2006).
174. K. Winkel, W. Schustereder, I. Kohl, C. G. Salzmann, E. Mayer, and T. Loerting, *Proc. 11th Intl. Conf. on the Physics and Chemistry of Ice*, W. F. Kuhs, ed., RSC, Dorchester, U.K., 2007, pp. 641.
175. M. C. Bellissent-Funel, L. Bosio, A. Hallbrucker, E. Mayer, and R. Sridi-Dorbez, *J. Chem. Phys.* **97**, 1282 (1992).
176. D. D. Klug, C. A. Tulk, E. C. Svensson, and C. K. Loong, *Phys. Rev. Lett.* **83**, 2584 (1999).
177. J. L. Finney, A. Hallbrucker, I. Kohl, A. K. Soper, and D. T. Bowron, *Phys. Rev. Lett.* **88**, 225503 (2002).
178. J. A. Ripmeester, C. I. Ratcliffe, and D. D. Klug, *J. Chem. Phys.* **96**, 8503 (1992).
179. D. D. Klug, O. Mishima, and E. Whalley, *J. Chem. Phys.* **86**, 5323 (1987).
180. M. C. Bellissent-Funel, and L. Bosio, *J. Chem. Phys.* **102**, 3727 (1995).
181. M. C. Bellissent-Funel, *Europhys. Lett.* **42**, 161 (1998).
182. F. W. Starr, M.-C. Bellissent-Funel, and H. E. Stanley, *Phys. Rev. E* **60**, 1084 (1999).
183. M. C. Bellissent-Funel, J. Teixeira, and L. Bosio, *J. Chem. Phys.* **87**, 2231 (1987).
184. E. G. Ponyatovsky, V. V. Sinitsyn, and T. A. Pozdnyakova, *J. Chem. Phys.* **109**, 2413 (1998).
185. M. Sasai and E. Shiratani, *Nippon Kessho Gakkaishi* **40**, 101 (1998).
186. V. V. Sinitsyn, E. G. Ponyatovsky, A. I. Kolesnikov, U. Dahlborg, and M. Calvo-Dahlborg, *Solid State Ionics* **145**, 415 (2001).
187. E. L. Gromnitskaya, O. V. Stal'gorova, V. V. Brazhkin, and A. G. Lyapin, *Phys. Rev. B* **64**, 094205 (2001).

188. C. A. Tulk, C. J. Benmore, J. Urquidi, D. D. Klug, J. Neuefeind, B. Tomberli, and P. A. Egelstaff, *Science* **297**, 1320 (2002).
189. M. M. Koza, H. Schober, H. E. Fischer, T. Hansen, and F. Fujara, *J. Phys. Condens. Matt.* **15**, 321 (2003).
190. K. Winkel, E. Mayer, and T. Loerting, in press.
191. M. M. Koza, B. Geil, K. Winkel, C. Koehler, F. Czeschka, M. Scheuermann, H. Schober, and T. Hansen, *Phys. Rev. Lett.* **94**, 125506 (2005).
192. M. M. Koza, T. Hansen, R. P. May, and H. Schober, *J. Non-Cryst. Solids* **352**, 4988 (2006).
193. M. Scheuermann, B. Geil, K. Winkel, and F. Fujara, *J. Chem. Phys.* **124**, 224503/1 (2006).
194. O. Mishima and Y. Suzuki, *Nature* **419**, 599 (2002).
195. S. Klotz, T. Straessle, R. J. Nelmes, J. S. Loveday, G. Hamel, G. Rouse, B. Canny, J. C. Chervin, and A. M. Saitta, *Phys. Rev. Lett.* **94**, 025506 (2005).
196. O. Mishima and H. E. Stanley, *Nature* **396**, 329 (1998).
197. C. A. Tulk, C. J. Benmore, D. D. Klug, and J. Neuefeind, *Phys. Rev. Lett.* **96**, 149601 (2006).
198. C. G. Salzmann, E. Mayer, and A. Hallbrucker, *Phys. Chem. Chem. Phys.* **6**, 5156 (2004).
199. R. J. Nelmes, J. S. Loveday, T. Straessle, C. L. Bull, M. Guthrie, G. Hamel, and S. Klotz, *Nat. Phys.* **2**, 414 (2006).
200. T. Loerting, K. Winkel, and E. Mayer, in press.
201. G. P. Johari, *J. Chem. Phys.* **121**, 8428 (2004).
202. S. Sastry, P. G. Debenedetti, F. Sciortino, and H. E. Stanley, *Phys. Rev. E* **53**, 6144 (1996).
203. P. G. Debenedetti, *Nature* **392**, 127 (1998).
204. R. J. Hemley, L. C. Chen, and H. K. Mao, *Nature* **338**, 638 (1989).
205. O. Andersson, *Phys. Rev. Lett.* **95**, 205503 (2005).
206. O. Andersson and A. Inaba, *Phys. Rev. B* **74** (2006).
207. R. J. Speedy, *J. Phys. Chem.* **86**, 3002 (1982).
208. R. J. Speedy, *J. Phys. Chem.* **86**, 982 (1982).
209. P. H. Poole, F. Sciortino, U. Essmann, and H. E. Stanley, *Nature* **360**, 324 (1992).
210. H. E. Stanley, C. A. Angell, U. Essmann, M. Hemmati, P. H. Poole, and F. Sciortino, *Physica A* **206**, 1 (1994).
211. L. P. N. Rebelo, P. G. Debenedetti, and S. Sastry, *J. Chem. Phys.* **109**, 626 (1998).
212. C. A. Angell, *Science* **319**, 582 (2008).
213. J. S. Tse, D. M. Shaw, D. D. Klug, S. Patchkovskii, G. Vankó, G. Monaco, and M. Krisch, *Phys. Rev. Lett.* **100**, 095502 (2008).
214. J. C. Li and P. Jenniskens, *Planet. and Space Sci.* **45**, 469 (1997).
215. G. P. Johari, *J. Chem. Phys.* **112**, 8573 (2000).
216. B. Geil, M. M. Koza, F. Fujara, H. Schober, and F. Natali, *Phys. Chem. Chem. Phys.* **6**, 677 (2004).
217. H. Schober, M. M. Koza, A. Tolle, C. Masciovecchio, F. Sette, and F. Fujara, *Phys. Rev. Lett.* **85**, 4100 (2000).
218. O. Andersson and H. Suga, *Phys. Rev. B* **65**, 140201 (2002).
219. C. G. Salzmann, I. Kohl, T. Loerting, E. Mayer, and A. Hallbrucker, *Phys. Chem. Chem. Phys.* **5**, 3507 (2003).
220. A. Hallbrucker, E. Mayer, and G. P. Johari, *J. Phys. Chem.* **93**, 7751 (1989).
221. G. P. Johari, A. Hallbrucker, and E. Mayer, *J. Phys. Chem.* **94**, 1212 (1990).

222. E. Mayer, in *J. Mol. Struct.*, **250**, 403 (1991).
223. G. P. Johari, A. Hallbrucker, and E. Mayer, *Nature* **330**, 552 (1987).
224. A. Hallbrucker, E. Mayer, and G. P. Johari, *Philos. Mag. B*, **60**, 179 (1989).
225. I. Kohl, L. Bachmann, E. Mayer, A. Hallbrucker, and T. Loerting, *Nature* **435**, E1 (2005).
226. I. Kohl, L. Bachmann, A. Hallbrucker, E. Mayer, and T. Loerting, *Phys. Chem. Chem. Phys.* **7**, 3210 (2005).
227. M. Chonde, M. Brindza, and V. Sadtchenko, *J. Chem. Phys.* **125**, 094501/1 (2006).
228. G. P. Johari, *J. Chem. Phys.* **127**, 157101 (2007).
229. M. Fisher and J. P. Devlin, *J. Phys. Chem.*, **99**, 11584 (1995).
230. R. S. Smith and B. D. Kay, *Nature* **398**, 788 (1999).
231. R. S. Smith, Z. Dohnalek, G. A. Kimmel, K. P. Stevenson, and B. D. Kay, *Chem. Phys.*, **258**, 291 (2000).
232. S. M. McClure, E. T. Barlow, M. C. Akin, D. J. Safarik, T. M. Truskett, and C. B. Mullins, *J. Phys. Chem. B* **110**, 17987 (2006).
233. S. M. McClure, D. J. Safarik, T. M. Truskett, and C. B. Mullins, *J. Phys. Chem. B* **110**, 11033 (2006).
234. P. Jenniskens and D. F. Blake, *Astrophys. J.* **473**, 1104 (1996).
235. P. Jenniskens, S. F. Banham, D. F. Blake, and M. R. S. McCoustra, *J. Chem. Phys.* **107**, 1232 (1997).
236. N. Giovambattista, C. A. Angell, F. Sciortino, and H. E. Stanley, *Phys. Rev. Lett.* **93**, 047801/1 (2004).
237. Y. Yue and C. A. Angell, *Nature* **427**, 717 (2004).
238. C. A. Angell, *J. Phys. Condens. Matt.* **19**, 205112/1 (2007).
239. G. P. Johari, *Phys. Chem. Chem. Phys.* **2**, 1567 (2000).
240. D. D. Klug, *Nature* **420**, 749 (2002).
241. J. S. Tse and M. L. Klein, *Phys. Rev. Lett.* **58**, 1672 (1987).
242. A. I. Kolesnikov, V. V. Sinityn, E. G. Ponyatovsky, I. Natkaniec, and L. S. Smirnov, *Phys. B Condens. Matt.* **213-214**, 474 (1995).
243. H. Schober, M. Koza, A. Tolle, F. Fujara, C. A. Angell, and R. Bohmer, *Phys. B Condens. Matt.* **241-243**, 897 (1998).
244. C. A. Tulk, D. D. Klug, E. C. Svensson, V. F. Sears, and J. Katsaras, *Appl. Phys. A Mater. Sci. Proc.* **74**, S1185 (2002).
245. O. Andersson and A. Inaba, *J. Chem. Phys.* **122**, 124710/1 (2005).
246. N. I. Agladze and A. J. Sievers, *Phys. B Condens. Matt.* **316-317**, 513 (2002).
247. T. Strassle, A. M. Saitta, S. Klotz, and M. Braden, **93** (2004).
248. E. L. Gromnitskaya, O. V. Stal'gorova, A. G. Lyapin, V. V. Brazhkin, and O. B. Tarutin, *JETP Lett.* **78**, 488 (2003).
249. T. Strassle, S. Klotz, G. Hamel, M. M. Koza, and H. Schober, *Phys. Rev. Lett.* **99**, 175501/1 (2007).
250. G. P. Johari and O. Andersson, *Phys. Rev. B Condens. Matt. Mater. Phys.* **70**, 184108/1 (2004).
251. O. Andersson, *J. Phys. Cond. Matt.* **20**, 244115 (2008).
252. O. Mishima, *J. Chem. Phys.* **115**, 4199 (2001).
253. O. Mishima, *J. Chem. Phys.* **121**, 3161 (2004).
254. H. E. Stanley, S. V. Buldyrev, N. Giovambattista, E. La Nave, A. Scala, F. Sciortino, and F. W. Starr, in *New Kinds of Phase Transitions: Transformations in Disordered Substances*, Vol.

- NATO Science Series, Vol. 81*, V. V. Brazhkin, S. V. Buldyrev, V. N. Ryzhov, and H. E. Stanley, eds., Kluwer Academic Publishers, Dordrecht, Germany, 2002, p. 309.
255. A. Mujica, A. Rubio, A. Munoz, and R. J. Needs, *Rev. Mod. Phys.* **75**, 863 (2003).
256. E. Rapoport, *J. Chem. Phys.* **46**, 2891 (1967).
257. E. G. Ponyatovskii and O. I. Barkalov, *Mat. Sci. Rep.* **8**, 147 (1992).
258. C. A. Angell and C. T. Moynihan, *Metallurg. Mat. Transact. B* **31B**, 587 (2000).
259. C. T. Moynihan and C. A. Angell, *J. Non-Cryst. Solids* **274**, 131 (2000).
260. O. Shimomura, S. Minomura, N. Sakai, K. Asaumi, K. Tamura, J. Fukushima, and H. Endo, *Phil. Mag.* **29**, 547 (1974).
261. O. Shimomura, in *High Pressure and Low Temperature Physics*, C. W. Chu and J. A. Woollam, eds., Plenum Press, New York, 1978, p. 483.
262. M. Imai, T. Mitamura, K. Yaoita, and K. Tsuji, *High Press. Res.* **15**, 167 (1996).
263. S. K. Deb, M. Wilding, M. Somayazulu, and P. F. McMillan, *Nature* **414**, 528 (2001).
264. P. F. McMillan, M. Wilson, D. Daisenberger, and D. Machon, *Nat. Mat.* **4**, 680 (2005).
265. T. Morishita, *Phys. Rev. Lett.* **93**, 055503 (2004).
266. M. Durandurdu and D. A. Drabold, *Phys. Rev. B Condens. Matt.* **64**, 014101 (2001).
267. D. Daisenberger, M. Wilson, P. F. McMillan, R. Q. Cabrera, M. C. Wilding, and D. Machon, *Phys. Rev. B* **75**, 224118 (2007).
268. P. F. McMillan, M. Wilson, M. C. Wilding, D. Daisenberger, M. Mezouar, and G. N. Greaves, *J. Phys. Condens. Matter* **19**, 415101/1 (2007).
269. F. H. Stillinger and T. A. Weber, *Phys. Rev. B Condens. Matt.* **31**, 5262 (1985).
270. K. Tanaka, *Phys. Rev. B Condens. Matt.* **43**, 4302 (1991).
271. J. Freund, R. Ingalls, and E. D. Crozier, *J. Phys. Chem.* **94**, 1087 (1990).
272. E. Principi, A. Di Cicco, F. Decremps, A. Polian, S. De Panfilis, and A. Filipponi, *Phys. Rev. B* **69**, 201201 (2004).
273. M. Durandurdu and D. A. Drabold, *Phys. Rev. B* **66**, 041201 (2002).
274. J. Koga, K. Nishio, T. Yamaguchi, and F. Yonezawa, *J. Phys. Soc. Jpn.* **73**, 388 (2004).
275. S. Goedecker and L. Colombo, *Phys. Rev. Lett.* **73**, 122 (1994).
276. M. H. Bhat, V. Molinero, E. Soignard, V. C. Solomon, S. Sastry, J. L. Yarger, and C. A. Angell, *Nature* **448**, 787 (2007).
277. S. Ansell, S. Krishnan, J. J. Felten, and D. L. Price, *J. Phys. Condens. Matt.* **10**, L73 (1998).
278. H. Kimura, M. Watanabe, K. Izumi, T. Hibiya, D. Holland-Moritz, T. Schenk, K. R. Bauchspiess, S. Schneider, I. Egry, K. Funakoshi, and M. Hanfland, *Appl. Phys. Lett.* **78**, 604 (2001).
279. N. Jakse, L. Hennet, D. L. Price, S. Krishnan, T. Key, E. Artacho, B. Glorieux, A. Pasturel, and M.-L. Saboungi, *Appl. Phys. Lett.* **83**, 4734 (2003).
280. T. H. Kim, G. W. Lee, B. Sieve, A. K. Gangopadhyay, R. W. Hyers, T. J. Rathz, J. R. Rogers, D. S. Robinson, K. F. Kelton, and A. I. Goldman, *Phys. Rev. Lett.* **95**, 085501/1 (2005).
281. K. Higuchi, K. Kimura, A. Mizuno, M. Watanabe, Y. Katayama, and K. Kuribayashi, *Meas. Sci. Technol.* **16**, 381 (2005).
282. K. Ohsaka, S. K. Chung, W. K. Rhim, and J. C. Holzer, *Appl. Phys. Lett.* **70**, 423 (1997).
283. W. K. Rhim, S. K. Chung, A. J. Rulison, and R. E. Spjut, *Int. J. Thermophys.* **18**, 459 (1997).
284. M. Langen, T. Hibiya, M. Eguchi, and I. Egry, *J. Cryst. Growth* **186**, 550 (1998).
285. W. K. W. K. Rhim and K. Ohsaka, *J. Cryst. Growth* **208**, 313 (2000).

286. Z. Zhou, S. Mukherjee, and W.-K. Rhim, *J. Cryst. Growth* **257**, 350 (2003).
287. T. Morishita, *Phys. Rev. Lett.* **97**, 165502/1 (2006).
288. S. Sastry and C. A. Angell, *Nat. Mat.* **2**, 739 (2003).
289. T. Morishita, *Phys. Rev. E* **77**, 020501/1 (2008).
290. P. Beaucage and N. Mousseau, *J. Phys. Condens. Matt.* **17**, 2269 (2005).
291. T. Morishita, unpublished.
292. A. Filipponi and A. Di Cicco, *Phys. Rev. B* **51**, 12322 (1995).
293. J. Koga, K. Nishio, T. Yamaguchi, and F. Yonezawa, *J. Phys. Soc. Jpn.* **73**, 136 (2004).
294. N. Funamori and K. Tsuji, *Phys. Rev. Lett.* **88**, 255508 (2002).
295. K. Tsuji, T. Hattori, T. Mori, T. Kinoshita, T. Narushima, and N. Funamori, *J. Phys. Condens. Matter* **16**, S989 (2004).
296. M. Ohtani, K. Tsuji, H. Nosaka, N. Hosokawa, and N. Funamori, *Proc. 17th AIRAPT Conference, Hawaii 1999*, p. 498.
297. A. Delisle, D. J. Gonzalez, and M. J. Stott, *J. Phys. Condens. Matt.* **18**, 3591 (2006).
298. T. Morishita, *Phys. Rev. E* **72**, 021201 (2005).
299. C. A. Angell, E. D. Finch, L. A. Woolf, and P. Bach, *J. Chem. Phys.* **65**, 3063 (1976).
300. F. X. Prielmeier, E. W. Lang, R. J. Speedy, and H. D. Ludemann, *Phys. Rev. Lett.* **59**, 1128 (1987).
301. I. Kushiro, *J. Geophys. Res.* **81**, 6347 (1976).
302. I. Kushiro and H. S. Yoder, Jr., B. O. Mysen, *J. Geophys. Res.* **81**, 6351 (1976).
303. G. H. Wolf and P. F. McMillan, in *Reviews in Mineralogy*, J. F. Stebbins, P. F. McMillan, and D. B. Dingwell, eds., Mineralogical Society of America, Washington, DC, 1995, p. 505.